Electronic Supplementary Information to accompany:

Predicting Valence Tautomerism in Diverse Cobalt-Dioxolene Complexes: Elucidation of the Role of Ligands and Solvent

F. Zahra M. Zahir, Moya A. Hay, Jett T. Janetzki, Robert W. Gable, Lars Goerigk* and Colette Boskovic*

*Email: c.boskovic@unimelb.edu.au, lars.goerigk@unimelb.edu.au

School of Chemistry, University of Melbourne, Victoria 3010, Australia

Contents

1. Computational Details[1]

Geometry Optimisation

Starting molecular structural coordinates were obtained using the crystal structures of available complexes and closely related analogues for other complexes. For all monocationic complexes (45 complexes) molecular geometry optimisations were carried out in gas phase with the computationally inexpensive GGA functional BP86 and the triple-ζ def2-TZVP atomic orbital basis set with Grimme's DFT-D3 dispersion correction with Becke-Johnson damping D3(BJ). The spin-unrestricted formalism was used for the open shell HS-Co^{II}-sq tautomer. For monocationic complexes, we used the singlet state to represent the LS-Co^{III}-cat form and quintet state for the HS-Co^{II}-sq form. Structures for the five neutral complexes geometries were taken from our previous study,[1] in which the doublet state represents the LS-Co^{III}-(cat)(sq) tautomer and the sextet state the HS-Co^{II}-$(sq)_2$ tautomer.

For the neutral complexes geometries, the already published ones were taken, which had been optimized with the hybrid composite approach PBEh-3c, which has a high amount of Fock exchange to prevent spin-delocalisation between the two dioxolene units. Since monocationic complexes contain only a single dioxolene unit, the tendency for a delocalisation of spin density is minimal. Hence, given the large number of data set and tunability in the basis set for the utilise of relativistic effects, BP86-D3(BJ)/def2-TZVP method is selected over the more expensive hybrid PBEh-3c method for cationic complexes.

After each geometry optimisation process a frequency analysis was performed. In all cases, the absence of any imaginary frequencies was ensured to verify that the structure was a true minimum.

---

[1] citations of the methods that have already appeared in the main article will not be repeated.

Geometry optimisations were performed using grid-4 or defgrid2 and the resolution of identity (RI) approximation with appropriate auxiliary basis functions employed. Spin-density distribution was obtained using the orca_plot program and generated using Chemcraft software[2] with standard defaults.

Quasi-Experimental Energies

For the initial development of the benchmark, calculation of solvent corrections (ΔE_S) for complexes **1–6** utilised the CPCM solvent model. In order to determine the parameter ΔE_S, the energy difference between the LS-Co^{III}-cat and HS-Co^{II}-sq tautomers was calculated in the gas phase (ΔE_{Gas}) as shown in equation S1.

$$\Delta E_{Gas} = E(\text{HS-Co}^{II}\text{-sq})_{gas} - E(\text{LS-Co}^{III}\text{-cat})_{gas} \tag{S1}$$

The energy difference between the LS-Co^{III}-cat and HS-Co^{II}-sq tautomers was then calculated by using the CPCM solvent model to obtain $\Delta E_{Solvent}$, as indicated in equation S2.

$$\Delta E_{Solvent} = E(\text{HS-Co}^{II}\text{-sq})_{Solvent} - E(\text{LS-Co}^{III}\text{-cat})_{Solvent} \tag{S2}$$

The energy differences with and without the solvent model were calculated to obtain the ΔE_S values for the required complexes as shown in equation S3.

$$\Delta E_S = \Delta E_{Solvent} - \Delta E_{Gas} \tag{S3}$$

BP86-D3(BJ)/def2-TZVP method was employed with acetonitrile (MeCN) with a dielectric constant (ε) of 37.50, 1,2-dichloromethane (DCM, $\varepsilon = 8.93$), and 1,2-dichloroethane (DCE, $\varepsilon = 10.36$) The ΔE_S values were also calculated as single point energies as well as geometry optimisations with and without the solvent model employed for further testing. The functional dependency was tested with various methods.

Relativistic corrections (ΔE_R) were calculated using BP86-D3(BJ) with the ZORA model. In order to determine the relativistic correction ΔE_R, the energy difference between the LS-Co^{III}-cat and HS-Co^{II}-sq tautomers was first calculated in the gas phase (ΔE_{Gas}) as shown in equation S1. The energy difference between the LS-Co^{III}-cat and HS-Co^{II}-sq tautomers was then calculated by incorporating relativistic effects to obtain $\Delta E_{Relativistic}$, as indicated in equation S4.

$$\Delta E_{Relativistic} = E(\text{HS-Co}^{II}\text{-sq})_{Relativistic} - E(\text{LS-Co}^{III}\text{-cat})_{Relativistic} \qquad (S4)$$

The energy differences with and without the relativistic model were calculated to obtain the ΔE_R values for the required complexes as shown in equation S5.

$$\Delta E_R = \Delta E_{Relativistic} - \Delta E_{Gas} \qquad (S5)$$

Calculations were performed with relativistically recontracted ZORA-def2-TZVPP basis set along with the segmented all electron relativistically recontracted SARC/J basis set[3] employing the largest numerical quadrature grid (Grid-7 or defgrid3). Relativistic corrections were also calculated as single point energies as well as geometry optimisations with and without the ZORA model for further testing. While method dependency was tested with various methods, the model dependency was tested by performing the calculations with Douglas-Kroll-Hess (DKH) Hamiltonian model.[4]

Thermal corrections (ΔE_T) were obtained with BP86-D3(BJ)/def2-TZVP at specified temperatures for complexes **1–6** in gas phase. Thermal corrections (ΔE_T) include thermal vibrational effects and zero-point energy differences between the two tautomers. Functional dependency was tested with the B97-3c GGA approach, which uses its own triple-ζ basis set.

Finally, the parameters ΔE_S, ΔE_R and ΔE_T were determined for complexes **1–6** and subtracted from the respective experimental enthalpy changes ΔH of the complexes to acquire quasi-experimental energies (ΔQE) as shown in equation S6 (or equation 1 of the main text).

$$\Delta QE = \Delta H - (\Delta E_S + \Delta E_R + \Delta E_T) \tag{S6}$$

Single Point Energy Calculations

Single point calculations were performed for the model complexes with fully polarised def2-TZVPP basis set in gas phase with 21 different functionals paired with various dispersion corrections that are listed in **Table 1** of the main text. The deviation/error of the functional from the quasi-experimental values were individually calculated for complexes **1–6.** The eight quasi experimental values determined for the six complexes (including three various experimental conditions of complex **6**) were averaged to obtain both mean absolute error (MAE) and mean signed error (MSE) as shown in equation S7 and S8 respectively, where ΔE_{Gas} are the calculated values for a given functional:

$$\text{MAE} = \frac{\sum |\Delta E_{Gas} - \Delta QE|}{8} \tag{S7}$$

$$\text{MSE} = \frac{\sum (\Delta E_{Gas} - \Delta QE)}{8} \tag{S8}$$

The option grid-4/defgrid2 was used for all functionals with the exception of the Minnesota functional M06L which can suffer from a higher grid dependence. In this case grid-7/defgrid3 was used. The resolution of identity (RI) approximation was used for the Coulomb integrals of the GGA and meta-GGA functionals with the appropriate auxiliary basis set[5,6] and in combination with the chain-of-sphere approximation for exchange (RIJCOSX)[7] for hybrid functionals, except for the range-separated hybrids ωB97M-D3(BJ) and ωB97X-D3(BJ) for which no RI techniques were employed.

Calculations for Solvent Effects

Calculations of solvent stabilisation energies/solvent corrections (ΔE_S) were conducted with M06L-D4/def2-TZVPP with defgrid-3 for both neutral and monocationic complexes using the CPCM solvent model with the default Gaussian vdW type surface, as implemented in ORCA 5.0.3. CPCM solvent model with MeCN (ε=37.50), DCM, (ε = 8.93), DCE (ε=10.36), butyronitrile (BuCN, ε = 20.30), acetone (ε = 20.70) and toluene (ε = 2.40) were used for relevant complexes. Relativistic corrections (ΔE_R) were also calculated with M06L-D4/ZORA-def2-TZVPP along with SARC/J basis set and grid-7/defgrid-3 for both neutral and cationic complexes. Thermal corrections (ΔE_T) for monocationic complexes were obtained with BP86-D3(BJ)/def2-TZVP whereas ΔE_T for neutral complexes obtained with PBEh-3c (at 298 K except for monocationic model complexes **5** and **6**).

2. Experimental and Synthetic Methods

Synthesis

Materials and methods. All synthesis were performed under a nitrogen atmosphere using standard Schlenk line techniques if not indicated otherwise. All chemicals were of reagent grade and were used as received, except for catechol which was recrystallised in toluene. Methanol was dried over 3 Å sieves and degassed by performing a minimum of ten cycles of vigorous shaking under vacuum and back-filling with nitrogen. The 3 Å sieves were activated by heating at 300 °C for 48 hours, followed by cooling under vacuum. Ferrocenium tetraphenylborate, ($FeCp_2.BPh_4$) and bis((6-methyl-2-pyridyl)methyl)(2-pyridylmethyl)amine (Me_2tpa) were synthesised based on literature procedures.[8,9] Synthesised $FeCp_2.BPh_4$ was stored at -25 °C under a nitrogen atmosphere.

[Co(H₄diox)(Me₂tpa)].BPh₄ (**15.BPh₄**). A solution of $CoCl_2.6H_2O$ (0.20 mmol, 47.6 mg), and Me_2tpa (0.20 mmol, 63.6 mg) in dried, degassed methanol (10 mL) was left stirring for 10 minutes under nitrogen to obtain a green solution. A second colourless solution containing catechol (0.20 mmol, 21.1 mg) was deprotonated with triethylamine (0.40 mmol, 55 µL) in methanol (10 mL) and stirred for 10 minutes. The deprotonated catechol was slowly added to the cobalt mixture resulting in an immediate orange-red solution that was left to stir for another 10 minutes. To the resulting solution, solid $FeCp_2.BPh_4$ (0.20 mmol, 101.1 mg) was added and sonicated for 15 minutes to obtain a greyish green precipitate. The mixture was then stirred for 3 hours, and the microcrystalline crude product was washed with methanol and diethylether and collected by vacuum filtration under atmospheric conditions. Synthetic attempts with $FeCp_2.PF_6$, or aerial oxidation followed by addition of $NaBPh_4$ or KPF_6 were unsuccessful. Yellow-green single crystals of diffraction quality were obtained by layering a very diluted solution of DCM with ample amount of hexane. Increased concentrations caused crystal deteriorations. To obtain a bulk sample a minimal concentration of the compound

dissolved in DCM was layered in round-bottom flask and slowly stirred with successive addition of hexane. Anal. Calcd for $C_{50}H_{46}N_4O_2BCo$: C, 74.63; H, 5.76; N, 6.96. Found C, 74.42; H, 5.84; N, 6.89. TGA data are consistent with no solvation.

[Co(4-tbdiox)(Me₂tpa)].BPh₄ **(19.BPh₄)** A solution of $CoCl_2.6H_2O$ (0.20 mmol, 47.6 mg), and Me₂tpa (0.20 mmol, 63.6 mg) in dried, degassed methanol (10 mL) was left stirring for 10 minutes under nitrogen to obtain a green solution. A colourless solution containing 4-*tert*-butylcatechol (0.20 mmol, 33.2 mg) was deprotonated with triethylamine (0.40 mmol, 55 μL) in methanol (10 mL) and stirred for 10 minutes. The deprotonated 4-*tert*-butylcatechol solution was slowly added to the cobalt mixture resulting in an immediate reddish-brown solution that was stirred for 10 minutes. Solid FeCp₂.BPh₄ (0.20 mmol, 101.1 mg) was added to the resulting solution and the solution was sonicated for 15 minutes followed by stirring for 3 hours to obtain a black-purple precipitate. The product was washed with diethyl ether and collected by vacuum filtration under atmospheric conditions. Black-purple single crystals of diffraction quality were obtained by layering DCM solution with hexane. A crystalline bulk sample was obtained by layering a solution of DCM with hexane. Anal. Calcd for $C_{54}H_{54}N_4O_2BCo$: C, 75.35; H, 6.32; N, 6.51. Found C, 75.28; H, 6.61; N, 6.43. TGA data are consistent with no solvation.

[Co(4-tbdiox)(tpa)].BPh₄ **(17.BPh₄)** A solution of $CoCl_2.6H_2O$ (0.20 mmol, 47.6 mg), and tpa (0.20 mmol, 58.7 mg) in dried, degassed methanol (10 mL) was left stirring for 10 minutes under nitrogen to obtain a green solution. A colourless solution containing 4-*tert*-butylcatechol (0.20 mmol, 33.2 mg) was deprotonated with triethylamine (0.40 mmol, 55 μL) in methanol (10 mL) and stirred for 10 minutes. Addition of deprotonated 4-*tert*-butylcatechol solution to the cobalt mixture resulted an

emerald-green solution that was left to stir for 10 minutes. Then, solid $FeCp_2.BPh_4$ (~0.20 mmol, 99.8 mg) was added and the solution was sonicated for 15 minutes followed by stirring for an hour to obtain a light-green precipitate. The crude product was collected by vacuum filtration under atmospheric conditions. Green needle-like crystals with diffraction quality were obtained from layering a solution of DCM with hexane. A crystalline bulk sample was obtained by layering a solution of DCM with hexane which was consistent with the formula [Co(tpa)(4-tbdiox)].BPh_4 (**17.BPh₄**). Anal. Calcd for $C_{54}H_{54}N_4O_2BCo$: C, 75.0; H, 6.05; N, 6.73. Found C, 74.93; H, 6.08; N, 6.77. Both elemental analysis and TGA data are consistent with this observation of no trapped solvent in the bulk sample due to a rapid solvent loss.

X-ray Data Collection and Structure Solution

Single-crystal X-ray diffraction data were obtained at the Australian Synchrotron at the MX1[10] and MX2[11] beamlines fitted with a silicon double crystal monochromator and Dectris Eiger 16M detector. For **15.BPh₄** and **19.BPh₄** data were collected at varying temperatures at the MX1 and MX2 beamlines respectively, while data for **17.BPh₄**·0.75DCM was acquired only at 100 K at the MX2 beamline. The wavelength was tuned to approximate Mo-Kα radiation ($\lambda = 0.710747$ Å for the data of **15.BPh₄** and **19.BPh₄**; $\lambda = 0.710925$ Å for **17.BPh₄**·0.75DCM). Data reduction was performed with XDS[12] using multi-scan absorption corrections carried out using SADABS.[13] Using Olex2,[14] the structure was solved with the ShelXT,[15] structure solution program using Intrinsic Phasing and refined with the ShelXL,[16] refinement package using Least Squares minimisation on F^2, using all data. All non-hydrogen atoms were refined with anisotropic displacement parameters, while all hydrogen atoms were placed at geometrical estimates and refined using the riding model with an isotropic

displacement parameter of 1.5Ueq of the parent atom, for all methyl carbon atoms, and 1.2Ueq of the parent atom, for all other atoms.

Powder X-ray diffraction (PXRD) data were measured on the Rigaku XtaLAB Synergy-S Dual Microfocus X-ray diffractometer using Cu-Kα (λ = 1.5418 Å) at 100 K for **15.BPh4** and **19.BPh4** and at 298 K for **17.BPh4**. Powder samples for all three compounds were prepared by gently crushing the sample and loading them into a 0.5 mm borosilicate glass capillary for measurement. Data were collected at 2θ = 5–50° with an exposure time of 60 s per frame and processed using CrysAlisPro[17] with an automated baseline correction.

Solid-State Magnetic Measurements

Magnetic measurements were performed on a Quantum Design SQUID MPMS3 magnetometer. Microcrystalline samples were loaded in VSM plastic capsules loaded on a brass sample holder. The magnetic susceptibility data were acquired under the application of 1 kOe magnetic field in the temperature range of 2–400 K. Each sample was collected by measuring upon cooling from 300 K to 2 K and upon heating to the maximum temperature (400 K) before being measured upon cooling to 2 K and then heating back up to the maximum temperature to study reversibility. The data were corrected for the diamagnetic contribution of the plastic capsule and brass holder, and of the sample using Pascal's constants.[18]

Electrochemistry

Electrochemical measurements were performed in MeCN at room temperature using a standard three-electrode configuration connected to an eDAQ computer-controlled potentiostat. Measurements were performed under a continuous nitrogen flow. The three-electrode system for cyclic voltammetry

consisted of a 1.0 mm diameter glassy carbon electrode (Cypress Systems), a platinum wire auxiliary electrode and a commercially available Ag/AgCl reference electrode (eDAQ). For rotating disk electrode (RDE) voltammetry, a 3 mm glassy carbon mounted on a Metrohm rotator was used. Analyte solutions with 1.0 mM concentration were prepared with 0.1 M BuN_4PF_6 supporting electrolyte. All potentials were referenced to the ferrocene/ferrocenium (Fc/Fc^+) couple measured at the same conditions immediately afterward.

Electronic Absorption Spectroscopy

Ultraviolet-visible (UV-vis) absorption spectra were recorded in the range 200–1100 nm on an Agilent Cary 3000 UV-vis spectrophotometer in built with a multi cell Peltier. Solution stability and insensitivity to oxygen was established in all cases by measuring unchanged spectra after several hours. Thermal stability of the complexes was confirmed by re-measuring room temperature spectra after heating and cooling. Absorption spectra for **17** were recorded in MeCN and BuCN. For **15** absorption spectra were acquired at varying temperatures in MeCN (268–333 K), DCM (268–303 K), DCE (268–348 K) BuCN (268–323 K) and acetone (268–318 K). Absorption spectra for **19** were recorded at varying temperatures in MeCN (268–333 K), BuCN (268–303 K) and acetone (268–318 K), DCE (268–313 K) and DCM (268–303 K).

Solution Magnetic Measurements

Solution magnetic measurements were measured by ^1H NMR spectroscopy according to the Evans method. Measurements were recorded on Bruker Ascend™ 400 MHz Spectrometer equipped with a BCUII temperature control. Solutions contained 0.5-2 % non-deuterated solvent as a standard.

Solution-based magnetic measurements for **15** were measured in DCM (253-298 K), MeCN (253–338 K), DCE (258–338 K) and acetone (258–313 K), while for **19** measurements were recorded in DCM (253–298 K), MeCN (253–338 K) and acetone (258–313 K). A solvent mixture was prepared containing deuterated solvent and 0.5–2 % non-deuterated solvent as a standard. The known mass of compounds for both **15** and **19** were dissolved in an accurately known volume of the solvent mixture to obtain a precise concentration and placed in an NMR tube. A coaxial NMR tube was placed with 70 μL of the same solvent mixture filled as an internal reference. The shift of the solvent mixture singlet peak compared to the paramagnetic solution peak ($\Delta\upsilon$) was measured in hertz. The mass magnetic susceptibility χ_g, can be calculated according to equation S9.

S9

$$\chi_g = \frac{3\Delta\upsilon}{4\pi m\upsilon} + \chi_0 + \chi_0 \frac{d_0 - d_s}{m}$$

Where υ is the spectrometer frequency (in Hz), χ_0 is the mass susceptibility of the solvent mixture, m is the mass concentration of the paramagnetic solution (in g cm^{-3}) corrected for the temperature dependence of the density of the solvent[19–21] (assuming deuterated and non-deuterated solvent mixtures have equal densities), d_0 is the density of pure solvent and d_s is the density of paramagnetic solution. As a dilute solution was used the following approximation can be made: ds = ds + m, which would result in a cancellation of the second and third terms of equation S9. The molar magnetic susceptibility χ_M was obtained by calculating the product of mass magnetic susceptibility multiplied by the molecular weight and then corrected for the diamagnetic contribution of the compound using Pascal's constants. The $\chi_M T$ values of each temperature were determined and the data for each solvent were fit to the regular solution model, (Equation S10).[22]

$$\chi_{\mathrm{M}}T = \left(\chi_{\mathrm{M}}T\right)_{min} + \frac{\left(\chi_{\mathrm{M}}T\right)_{max} - \left(\chi_{\mathrm{M}}T\right)_{min}}{1+\mathrm{e}^{\frac{\Delta S}{R}\left(\frac{T_{1/2}}{T}-1\right)}}$$

where $\left(\chi_{\mathrm{M}}T\right)_{max}$ and $\left(\chi_{\mathrm{M}}T\right)_{min}$ represents the minimum and maximum values of $\chi_{\mathrm{M}}T$ respectively, and R is the ideal gas constant with a value of 8.314 J K^{-1} mol^{-1}.

Each fit rendered the $T_{1/2}$, ΔH and ΔS values for complex **15** and **19** in the relevant solvents. (The maximum obtained $\chi_{\mathrm{M}}T$ values of **19.BPh4** in DCM was set as the maximum upper bound and the lowest obtained $\chi_{\mathrm{M}}T$ values in MeCN of **15.BPh4** were set as the minimum lower bound, while allowing a free fit for convergence to obtain the best data curve). This however results in relatively larger errors compared to a force fitted curve/fixed parameters. This approach is to illustrate the uncertainty in the experimental measurements of incomplete transitions.

Other Measurements

Elemental analyses (C, H, N) were performed at the Elemental Microanalytical Services, Macquarie University. Thermogravimetric analyses were performed by TRACEES at University of Melbourne on a PerkinElmer TGA 8000 instrument using a ramp rate of 5 °C per minute up to a maximum temperature of 450 °C under an N$_2$ atmosphere. Attenuated total reflectance infrared spectra were measured on a Bruker Alpha spectrometer and normalised as absorbance spectra.

3. DFT Results

Spin Density Distribution

We commenced the process using geometry optimisation of complexes **1–6**. BP86-D3(BJ) was chosen as it should provide reliable geometries, but careful examination of the resulting geometries for spin delocalisation was still required. A close analysis of the spin densities is suggestive of accurate spin localisation (**Fig. S1-S6**).
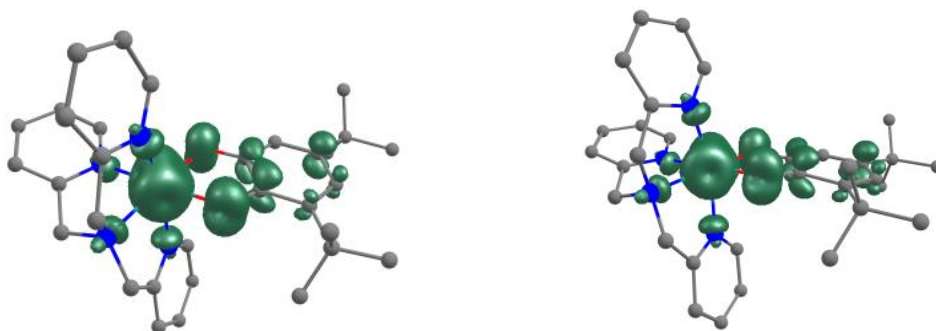
Fig. S1 Optimised geometry and spin density distribution (isovalue=0.008) of complex **1** for the HS-Co^{II}-sq state as calculated with BP86-D3(BJ)/def2-TZVP (left) and PBEh-3c (right). Both functionals give the expected spin densities, ruling out the delocalisation error for this system.
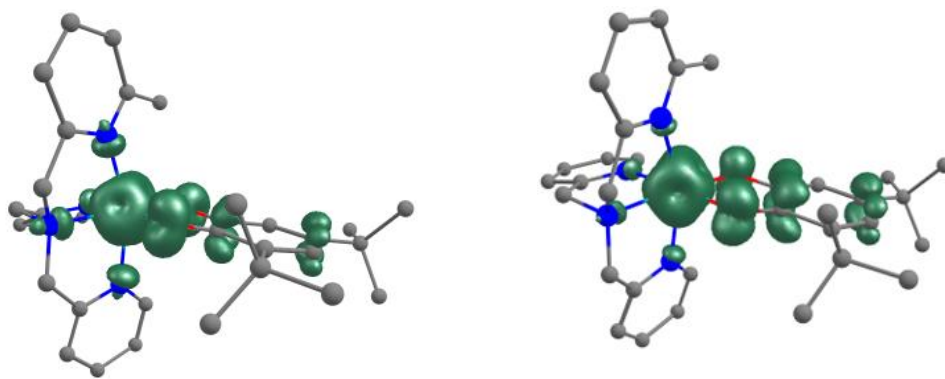
Fig. S2 Optimised geometry and spin density distribution (isovalue = 0.008) of complex **2** for the HS-Co^{II}-sq state as calculated with BP86-D3(BJ)/def2-TZVP (left) and PBEh-3c (right). Both functionals give the expected spin densities, ruling out the delocalisation error for this system.
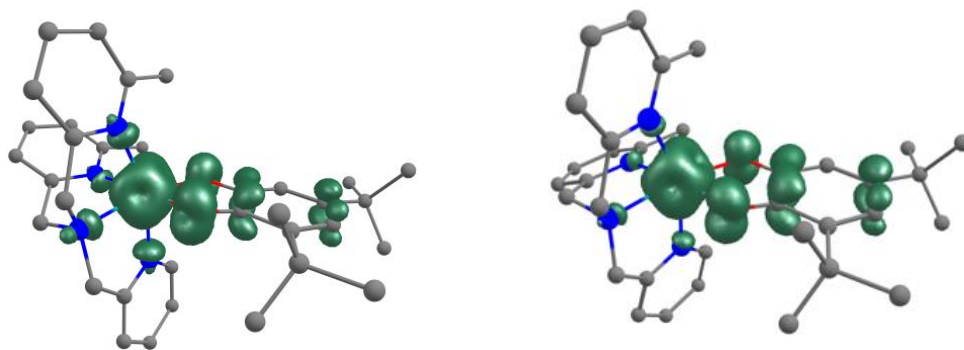
Fig. S3 Optimised geometry and spin density distribution (isovalue = 0.008) of complex **3** for the HS-Co^{II}-sq state as calculated with BP86-D3(BJ)/def2-TZVP (left) and PBEh-3c (right). Both functionals give the expected spin densities, ruling out the delocalisation error for this system.
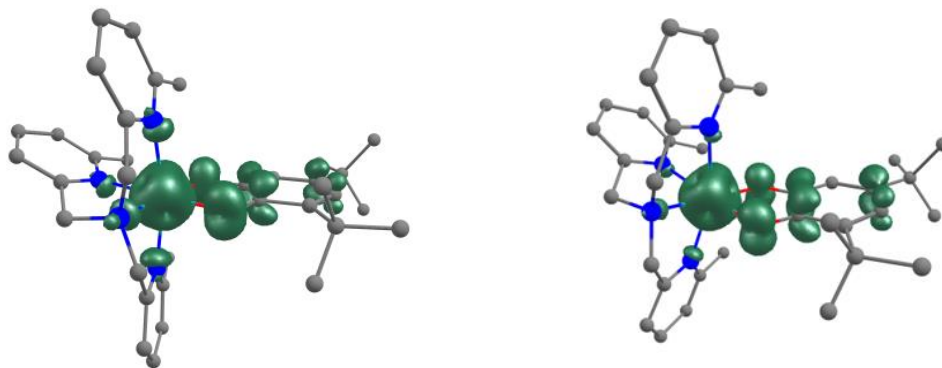
Fig. S4 Optimised geometry and spin density distribution (isovalue = 0.008) of complex **4** for the HS-Co^{II}-sq state as calculated with BP86-D3(BJ)/def2-TZVP (left) and PBEh-3c (right). Both functionals give the expected spin densities, ruling out the delocalisation error for this system.
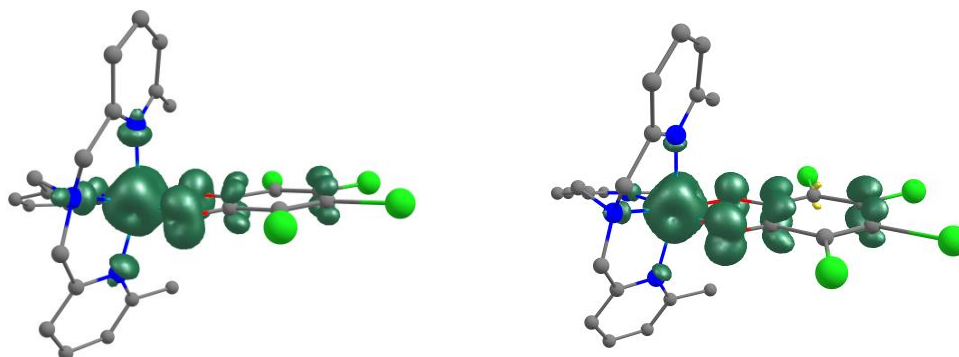
Fig. S5 Optimised geometry and spin density distribution (isovalue=0.008) of complex **5** for the HS-Co^{II}-sq state as calculated with BP86-D3(BJ)/def2-TZVP (left) and PBEh-3c (right). Both functionals give the expected spin densities, ruling out the delocalisation error for this system.
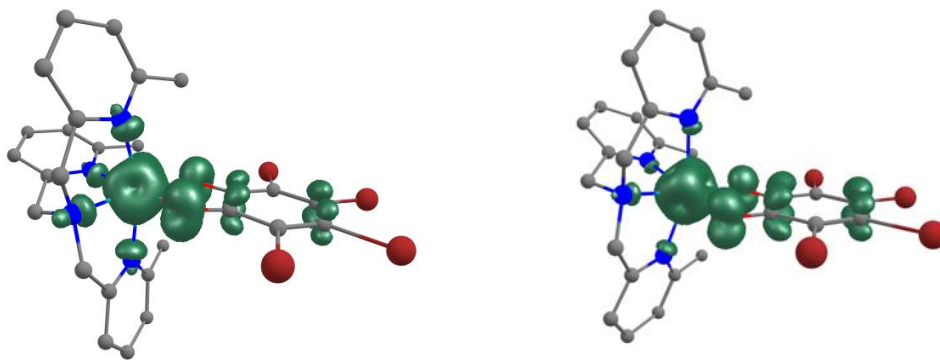
Fig. S6 Optimised geometry and spin density distribution (isovalue = 0.008) of complex **6** for the HS-Co^{II}-sq state as calculated with BP86-D3(BJ)/def2-TZVP (left) and PBEh-3c (right). Both functionals give the expected spin densities, ruling out the delocalisation error for this system.

Quasi-Experimental Energies

Simulating the chemical environment and other effects is crucial for reliable computational results but is challenging to handle in a large data set. Following geometric verification, the individual corrections for solvent (ΔE_S), relativistic (ΔE_R), and thermal effects (ΔE_T), were chosen for quantification (**Table S1–S3**). We calculated these effects for one complex with different methods and found the differences between approaches are far below the chemical accuracy threshold and, thus, negligible for our purposes (**Table S4–S6**). All the corrections reported here are based on single point calculations on the gas-phase optimised structures. Reoptimising the structures in the presence of a solvent or relativistic (ZORA) model had no significant difference compared to the single point-based approach (**Table S5–S6**).

Table S1. The solvent corrections (ΔE_S) obtained using CPCM model for each model complex calculated with BP86-D3(BJ)/def2-TZVP.

Model complex	Solvent	$\Delta E_{\text{(HS-CoII-sq - LS-CoIII-cat)}}$ / kJ mol^{-1}		ΔE_S / kJ mol^{-1}
		Solvent	Gas	
1[a]	MeCN	112.7	80.0	32.7
2[a]	MeCN	96.7	63.9	32.8
3[a]	MeCN	73.3	43.8	29.5
4[a]	MeCN	55.6	25.7	29.9
5[b]	DCM	76.9	44.6	32.3
6[a]	DCM	82.4	49.7	32.7
	DCE	83.0	49.7	33.3
	MeCN	86.8	49.7	37.1

[a] Thermochemical parameter obtained using electrochemistry measurements in MeCN. [b] VT transitions reported in multiple solvents.

Table S2. The relativistic corrections (ΔE_R) obtained using the ZORA model for each model complex calculated with BP86-D3(BJ)/def2-TZVP.

Model complex	$\Delta E_{\text{(HS-CoII-sq - LS-CoIII-cat)}}$ / kJ mol^{-1}		ΔE_R / kJ mol^{-1}
	Relativistic[a]	Non-Relativistic	
1	91.8	80.0	11.8
2	75.0	63.9	11.1
3	54.6	43.8	10.8
4	35.5	25.7	9.8
5	54.8	44.6	10.2
6	59.1	49.7	9.4

[a] Relativistic correction calculated with ZORA/ZORA-def2-TZVP in gas phase for the geometries optimised in gas phase

Table S3. Thermal corrections (ΔE_T) (that includes thermal vibrations and zero-point energies) calculated with BP86-D3(BJ)/def2-TZVP.

Model complex	T / K	ΔE_T / kJ mol^{-1}
1[a]	298	-3.7
2[a]	298	-5.4
3[a]	298	-3.5
4[a]	298	-3.0
5[b]	250	-5.7
6[c]	291	-5.3
	295	-5.2
	359	-4.6

[a] Thermochemical parameter obtained using electrochemistry measurements at 298 K. [b] Estimated switching point. [c] Thermal corrections calculated at three different VT transition temperatures ($T_{1/2}$) of complex **6**.

Table S4. Thermal corrections (ΔE_T) (that includes thermal vibrations and zero-point energies) calculated with BP86-D3(BJ)/def2-TZVP and B97-3c in gas phase for complex **5**.

Method	T / K	ΔE_T / kJ mol^{-1}
BP86-D3(BJ) / def2-TZVP	250	-5.7
B97-3c	250	-5.6

Table S5. Solvent corrections (ΔE_S) calculated for complex **5** calculated as geometry or single point energies as well with different methods (tests for method dependencies).

Method	Calculation Geometry / Single point	$\Delta E_{\text{(HS-CoII-sq - LS-CoIII-cat)}}/$ kJ mol^{-1}	ΔE_S / kJ mol^{-1}
BP86-D3(BJ) /	Gas / Gas[a]	44.6	-
Def2-TZVP	Gas / DCM[b]	76.9	32.3
(CPCM)	DCM / DCM[c]	78.0	33.4
B97-3c / def2-mTZVP	Gas / Gas[a]	0.9	
(CPCM)	Gas / DCM[b]	32.9	32.0
	DCM / DCM	33.4	33.1

[a] Energy calculations in gas phase for geometry optimised in gas phase. [b] Energy calculations in DCM (CPCM model) for geometry optimised in gas phase. [c] Energy calculations in DCM (CPCM model) for geometry optimised in DCM (CPCM model).

Table S6. Relativistic corrections (ΔE_R) calculated for complex **5** calculated with ZORA model and DKH model as geometry or single point energies with different methods (tests for model and method dependencies).

Method		ΔE_R (ZORA) / kJ mol^{-1}	ΔE_R (DKH) / kJ mol^{-1}
TPSS	Single point[a]	11.1	10.4
B97M-V	Single point[a]	11.6	10.8
BP86-D3(BJ)	Single point[a]	10.2	9.4
BP86-D3(BJ)	Geometry[b]	9.6	-

[a] Relativistic correction calculated as single point energy. [b] Geometries optimised with the inclusion of a relativistic model.

Density Functional Benchmark for Spin-State Energies[2]

Despite the lack of a universally accurate functional for spin state energetics, general insights can be gained from previous studies.[23,24] Pure functionals belonging to the local density approximation or general gradient approximation (GGA) such as PBE[25], and BLYP[26–28] favour the low spin geometry,[29,30] whilst hybrid functionals like PBE0[31,32] M06[33] and B3LYP tend to over stabilise high-spin geometries. Different functionals may vary between 40–120 kJ mol^{-1} for transition metal spin state energetics,[34] which mandates the exploration of an appropriate functional. Hence, we chose a total of 21 combinations of functionals and dispersion corrections to assess (**Table 1** of the main text). The choice of methods was based on literature popularity or their general robust performance in various applications.[35–37] The MAEs of all tested methods relative to the quasi-experimental values for **1**–**6** at different conditions are shown in **Fig. S7** (See **Table S7–S8** and **Fig. S8** for individual errors of each method for each complex).

---

[2] The term "spin-state energetics" is employed for the discussion for certain parts of the discussion of computational analysis which represents valence tautomeric energy separation wherever relevant.
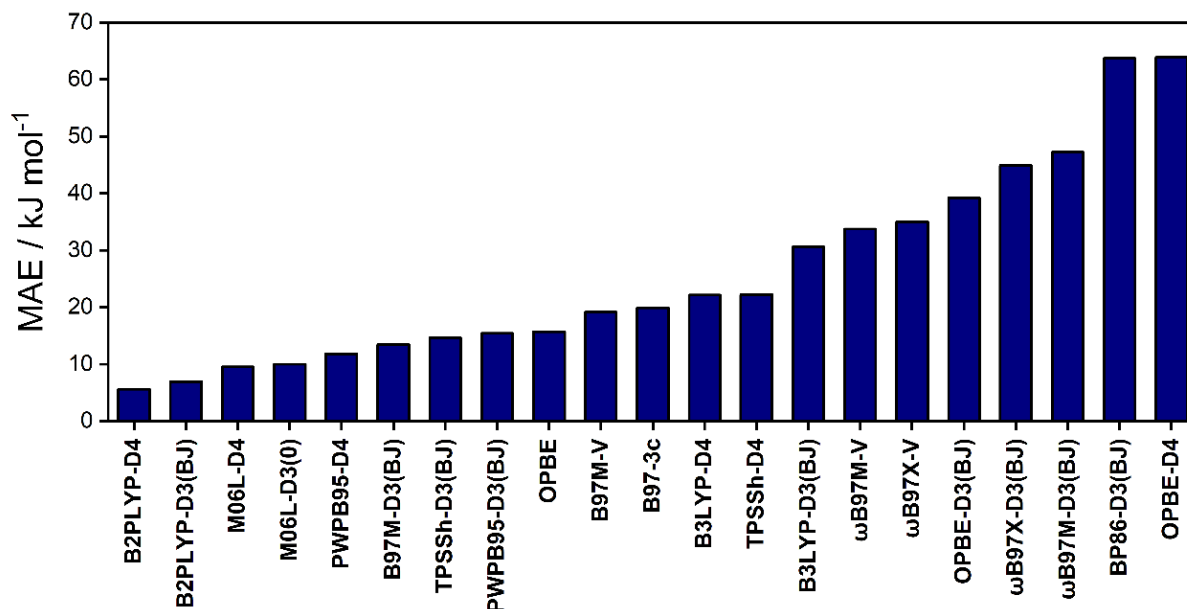
Fig. S7 Mean absolute errors (MAE) for spin-state energetics of the six reference [Co(Xdiox)(Me$_n$tpa)]$^+$ complexes (**1-6**) for several tested methods (def2-TZVPP basis set)

The functionals PWPB95-D3(BJ), PWPB95-D4, B97M-D3(BJ) and TPSSh-D3(BJ) performed moderately (MAE ranging from 11.8–15.4 kJ mol^{-1}), whilst the range-separated hybrids performed poorly (e. g., MAE of 47.2 kJ mol^{-1} for ωB97M-D3(BJ)). The BP86-D3(BJ) method, which is commonly used in similar calculations, provided an unsatisfactory MAE of 63.7 kJ mol^{-1} and seemingly over-stabilises the LS-Co^{III}-cat state; it is therefore incompatible for the calculation of spin-state energy seperations.[38] From the analysis, the double hybrid variants B2PLYP-D4 (MAE = 5.6 kJ mol^{-1}) and B2PLYP-D3(BJ) (MAE = 6.9 kJ mol^{-1}), and the meta-GGAs M06L-D4 (MAE = 9.5 kJ mol^{-1}) and M06L-D3(0) (MAE = 10.0 kJ mol^{-1}) are the standout performers with MAE below 10 kJ mol^{-1} and absolute mean signed errors (MSEs) below 2.5 kJ mol^{-1} (**Fig. S8**, **Table S8)**

Dispersion corrections applied to various functionals showed that dispersion effects cannot be neglected (**Table S9**). Among the tested functionals, M06L is the least affected by the corrections with an absolute average deviation between M06L and M06L-D4 being only 2.6 kJ mol^{-1}. The double hybrid functionals (including B2PLYP) showed a deviation between corrected and uncorrected methods from 9.5 to 12.5 kJ mol^{-1}. Hybrid functionals, such as B3LYP, showed an average impact by the dispersion correction of nearly 30 kJ mol^{-1}. OPBE, an extensively used functional in spin-state energetics, performed the worst when paired with dispersion corrections, with the MAE increasing from 15.7 kJ mol^{-1} for OPBE to 63.9 kJ mol^{-1} for OPBE-D4 (**Table S8**). This illustrates that in previous studies that have ignored the impact of London dispersion forces, recommendation of a specific functional, such as pure OPBE, might have relied on error compensation.

In summary, the double hybrid functional B2PLYP-D4 excelled in its ability to describe the 3d transition metal spin-state energetics outlined in this section, which is surprising owing to the high admixture of Fock exchange and the additional second-order perturbation theory component. The functional M06L-D4 also worked very well in this benchmark study, with a slightly better MSE compared to B2PLYP-D4 (**Table S8**). Owing to the remarkable performance of M06L-D4 in our recent benchmark of neutral [Co(3,5-dbdiox)(3,5-dbsq)(N$_2$L)], whereas B2PLYP-D4 performed only moderately in that study,[1] we have selected M06L-D4 over B2PLYP-D4 for the calculation and prediction of cationic Co-dioxolene complexes.

Table S7. Spin-state energy difference of reference complexes **1**–**6** calculated with each method.

Method[a]	spin-state energy difference (ΔE_{Gas})[b] / kJ mol⁻¹					
	1	**2**	**3**	**4**	**5**	**6**
B2PLYP-D4	19.6	-2.9	-21.5	-46.6	-13.0	-8.7
B2PLYP-D3(BJ)	16.2	-6.4	-24.9	-50.0	-16.8	-12.6
M06L-D4	16.1	-0.8	-16.5	-45.0	-14.2	-12.9
M06L-D3(0)	14.8	-2.2	-17.9	-42.1	-16.0	-14.2
PWPB95-D4	6.0	-16.1	-34.5	-58.8	-25.0	-20.1
B97M-D3(BJ)	30.6	10.7	-8.2	-28.2	-2.4	1.5
TPSSh-D3(BJ)	31.4	11.4	-7.4	-29.2	-0.8	3.7
PWPB95-D3(BJ)	1.5	-20.6	-39.1	-63.4	-29.4	-24.0
OPBE	19.0	-1.8	-21.8	-38.7	-29.4	-27.8
B97M-V	35.3	15.8	-2.5	-21.8	3.5	7.5
B97-3c	37.8	21.1	1.5	-16.2	0.6	4.9
B3LYP-D4	-7.5	-27.4	-45.8	-68.0	-35.0	-31.2
TPSSh-D4	38.6	18.5	-0.5	-22.3	7.1	11.8
B3LYP-D3(BJ)	-15.6	-35.5	-53.6	-75.7	-43.8	-40.2
ωB97M-V	-18.7	-41.2	-59.7	-84.0	-44.6	-40.4
ωB97X-V	-19.4	-42.3	-61.2	-86.4	-45.6	-41.7
OPBE-D3(BJ)	58.0	40.1	18.9	0.5	19.7	25.4
ωB97X-D3(BJ)	-28.6	-51.7	-71.0	-96.7	-55.5	-51.7
ωB97M-D3(BJ)	-32.8	-54.7	-72.5	-96.9	-58.0	-54.2
BP86-D3(BJ)	80.3	64.0	44.1	26.1	44.9	50.0
OPBE-D4	83.5	64.5	42.8	24.1	44.9	50.4

[a] Each method is calculated with def2-TZVPP in gas phase, while B97-3c is used with the def2-mTZP basis set. [b] ΔE_{Gas} is calculated as $E_{(HS-CoII-sq)} - E_{(LS-CoIII-cat)}$

Table S8. Mean absolute error (MAE) and mean signed error (MSE) of each complex (**1**–**6**) calculated with different methods with reference to the quasi-experimental energies.

Method[a]	Error of model complexes / kJ mol⁻¹								MSE	MAE
	1	**2**	**3**	**4**	**5**	**6**[c]				
	MeCN	MeCN	MeCN	MeCN	DCM	DCM	DCE	MeCN		
ΔQE^c (kJ mol⁻¹)	**20.2**	**-4.5**	**-30.8**	**-61.7**	**-5.8**	**-1.8**	**-5.5**	**-9.9**		
B2PLYP-D4	0.6	-1.6	-9.3	-15.1	7.2	6.9	3.2	-1.2	-1.2	5.6
B2PLYP-D3(BJ)	4.0	1.9	-5.9	-11.7	11.0	10.8	7.1	2.7	2.5	6.9
M06L-D4	4.1	-3.7	-14.3	-23.7	8.4	11.1	7.4	3.0	-1.0	9.5
M06L-D3(0)	5.4	-2.2	-14.9	-22.5	10.2	12.3	8.7	4.3	0.2	10.0
PWPB95-D4	14.2	11.6	3.7	-2.9	19.2	18.3	14.6	10.2	11.1	11.8
B97M-D3(BJ)	-10.4	-15.2	-22.6	-33.5	-3.4	-3.3	-7.0	-11.4	-13.4	13.4
TPSSh-D3(BJ)	-11.3	-15.9	-23.4	-32.5	-5.0	-5.5	-9.2	-13.6	-14.6	14.6
PWPB95-D3(BJ)	18.7	16.1	8.3	1.7	23.7	22.2	18.5	14.1	15.4	15.4
OPBE	1.1	-2.7	-9.0	-23.0	23.6	26.0	22.3	17.9	7.0	15.7
B97M-V	-15.1	-20.3	-28.3	-39.9	-9.3	-9.3	-13.0	-17.4	-19.1	19.1
B97-3c	-17.7	-25.6	-32.3	-45.5	-6.4	-6.7	-10.4	-14.8	-19.9	19.9
TPSSh-D4	-18.4	-23.0	-30.3	-39.4	-12.9	-13.6	-17.3	-21.7	-22.1	22.1
B3LYP-D4	27.7	22.9	15.0	6.3	29.2	29.4	25.7	21.3	22.2	22.2
B3LYP-D3(BJ)	35.8	31.0	22.8	14.0	38.0	38.4	34.7	30.3	30.6	30.6
ωB97M-V	38.9	36.7	28.9	22.3	38.8	38.6	34.9	30.5	33.7	33.7
ωB97X-V	39.6	37.8	30.4	24.7	39.8	39.9	36.2	31.8	35.0	35
OPBE-D3(BJ)	-37.8	-44.6	-49.7	-62.2	-25.5	-27.2	-30.9	-35.3	-39.2	39.2
ωB97X-D3(BJ)	48.8	47.2	40.2	35.0	49.7	49.9	46.2	41.8	44.9	44.9
ωB97M-D3(BJ)	53.0	50.2	41.7	35.2	52.2	52.4	48.7	44.3	47.2	47.2
BP86-D3(BJ)	-60.1	-68.5	-74.9	-87.8	-50.7	-51.8	-55.5	-59.9	-63.7	63.7
OPBE-D4	-63.3	-69.0	-73.6	-85.8	-50.7	-52.2	-55.9	-60.3	-63.9	63.9

[a] Each method is calculated with def2-TZVPP except for B97-3c which uses its own def2-mTZP basis set. [b] ΔQE obtained at relevant conditions. [c] For complex **6**, ΔQE obtained in three solvents at their transition temperatures (Table 1 of the main text)
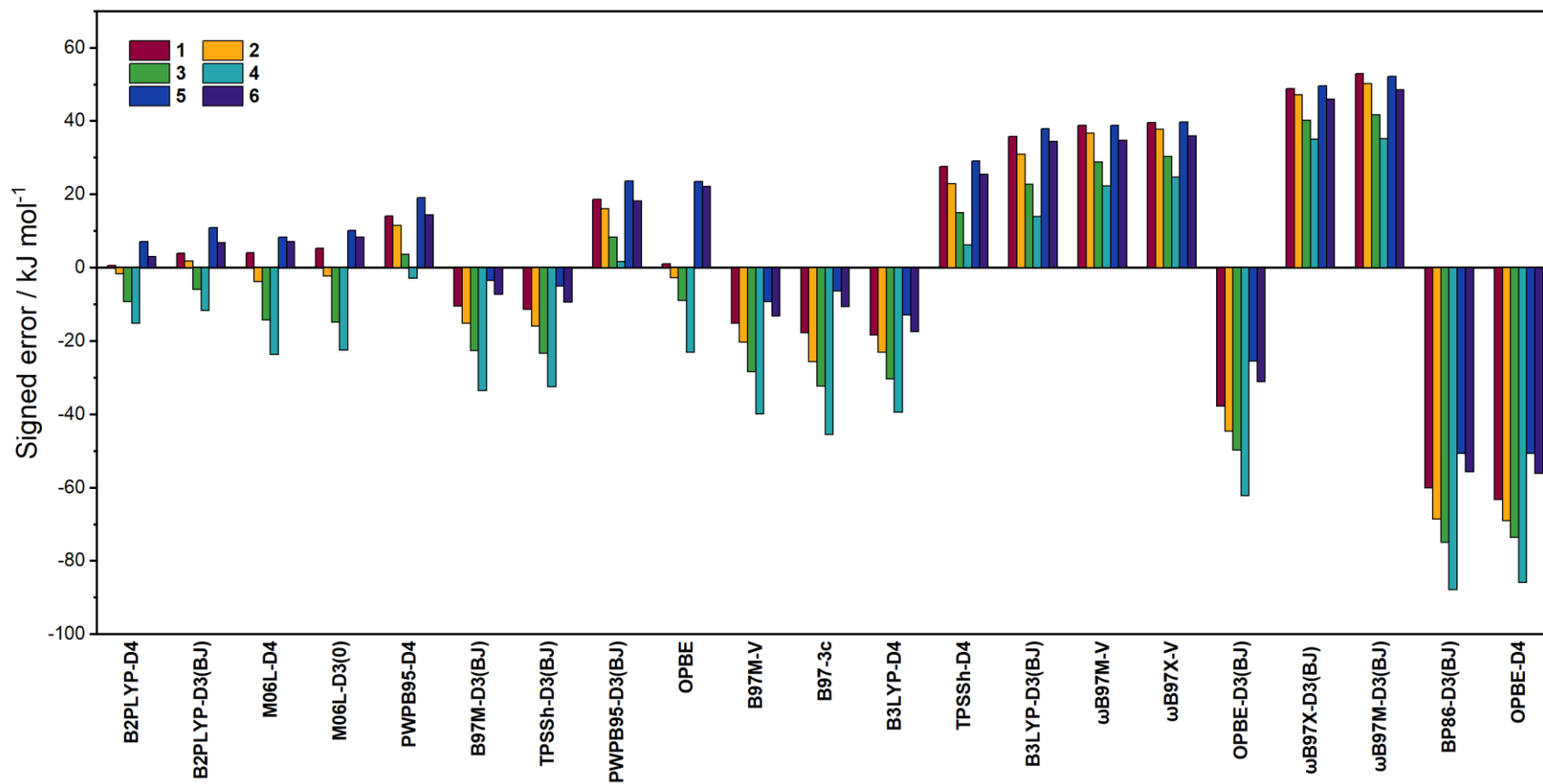
Fig. S8 Signed error of individual model complexes **1–6** calculated with different methods in gas phase (with def2-TZVPP basis set, except for B97-3c which uses its own def2-mTZP basis set)

Table S9. Effect of dispersion corrections tested for different functionals with def2/TZVPP in gas phase on complexes **1**–**6** with D4 dispersion and without dispersion corrections.

Functional/ Def2-TZVPP	Model Complex	$\Delta E_{\text{(HS-CoII-sq - LS-CoIII-cat)}}$/ kJ mol^{-1}			
		D4 dispersion corrections (D4)	No dispersion corrections (ND)	Deviation (D4-ND)	Average deviation
M06L	1	16.1	13.7	2.4	
	2	-0.8	-3.4	2.6	
	3	-16.5	-19.1	2.6	2.6
	4	-38.0	-40.5	2.5	
	5	-14.2	-16.8	2.6	
	6	-12.9	-15.7	2.8	
B2PLYP	1	19.6	8.5	11.1	
	2	-2.9	-15.1	12.2	
	3	-21.5	-33.1	11.6	12.5
	4	-46.6	-57.5	10.9	
	5	-13.0	-27.1	14.1	
	6	-8.7	-24.1	15.3	
OPBE	1	83.5	19.1	64.5	
	2	64.5	-1.8	66.3	
	3	42.8	-21.8	64.6	68.5
	4	24.1	-38.7	62.8	
	5	44.9	-29.4	74.3	
	6	50.4	-27.8	78.2	
TPSSh	1	38.6	19.2	19.4	
	2	18.5	-2.6	21.2	
	3	-0.5	-20.8	20.3	21.9
	4	-22.3	-41.4	19.1	
	5	7.1	-17.4	24.5	
	6	11.8	-14.8	26.6	
B3LYP	1	-7.5	-31.7	24.2	
	2	-27.4	-53.5	26.1	
	3	-45.8	-70.8	25.0	27.0
	4	-68.0	-91.7	23.7	
	5	-35.0	-65.3	30.3	
	6	-31.2	-64	32.8	
PWPB95	1	6.0	-2.9	8.9	
	2	-16.1	-25.5	9.4	
	3	-34.5	-43.7	9.2	9.5
	4	-58.8	-67.5	8.7	
	5	-25.0	-35.2	10.3	
	6	-20.1	-30.6	10.5	

Ligands Used in Monocationic Complexes

Table S10. Abbreviations and names of dioxolene ligands and N-donor ancillary ligands (**Chart 2**) employed in this work.

Dioxolene ligands used		Ancillary ligands used		
Abbreviation	Name	Type	Abbreviation	Name
3,5-dbdiox	3,5-di-*tert*-butyldioxolene	Me$_n$tpa	tpa (R$_1$=R$_2$=R$_3$=H)	tris(2-pyridylmethyl)amine
Cl$_4$diox	tetrachlorodioxolene		Metpa (R$_1$=R$_2$=H; R$_3$=CH$_3$)	(6-methyl-2-pyridylmethyl)bis(2-pyridylmethyl)amine
Br$_4$diox	tetrabromodioxolene		Me$_2$tpa (R$_1$=H; R$_2$=R$_3$=CH$_3$)	bis(6-methyl-2-pyridylmethyl)(2-pyridylmethyl)amine
H$_4$diox	1,2-dioxolene		Me$_3$tpa (R$_1$=R$_2$=R$_3$=CH$_3$)	tris(6-methyl-2-pyridylmethyl)amine
4-tbdiox	4-*tert*-butyldioxolene	Quinoline	bpqa	bis(2-pyridylmethyl)(2-quinolylmethyl)amine
Andiox	9-(3,4-dihydroxyphenyl)anthracene		pbqa	(2-pyridylmethyl)bis(2-quinolylmethyl)amine
dioxophen	9,10-dioxophenanthrene		tqa	tris(2-quinolylmethyl)amine
naphdiox	naphthalene-2,3-diol		*iso*-pbqa	(2-pyridylmethyl)bis(2-quinolylmethyl)amine
esc	6,7-dihydroxycoumarin (esculetin)		*iso*-tqa	tris(2-isoquinolylmethyl)amine
3,6-dbdiox	3,6-di-*tert*-butyldioxolene	Pyrazole	PzPy$_2$	(3,5-dimethyl-1H-pyrazol-1-yl)-N,N-bis(pyridin-2-ylmethyl)methanamine
			Pz$_2$Py	3,5-dimethyl-1H-pyrazol-1-yl)-N-((3,5-dimethyl-1H-pyrazol-1-yl)methyl)-N-(pyridine-2-yl-methyl)methanamine
			Pz$_3$	tris((3,5-dimethyl-1H-pyrazol-1-yl)methyl)amine
			bmimapy	(bis(1-methylimidazol-2-yl)methyl)(2-(pyridyl-2- yl)ethyl)amine
		AzaN	iPr$_2$AzaN [R=CH(CH$_3$)$_2$]	N,N′-diisopropyl-2,11-diaza[3.3]-(2,6)pyridinophane
			Et$_2$AzaN (R=CH$_2$CH$_3$)	N,N′-diethyl-2,11-diaza[3.3]-(2,6)pyridinophane
			Me$_2$AzaN (R=CH$_3$)	N,N′-dimethyl-2,11- diaza[3.3]-(2,6)pyridinophane
		Cyclam	cth	dl-5,7,7,12,14,14-hexamethyl-1,4,8,11-tetraazacyclotetradecane
			cyclam	1,4,8,11-tetraazacyclotetradecane
			Me$_4$cyclam	1,4,8,11-tetramethylcyclotetradecane
		Other	tren	tris(2-aminoethyl)amine
			Py$_2$en	N,N'-bis(pyridin-2-ylmethyl)ethylenediamine

Table S11. Electronic energies of the complexes in gas phase obtained with M06L-D4/def2-TZVPP

Complexes	$E(\text{LS-Co}^{\text{III}}\text{-cat})$ / E_h	$E(\text{HS-Co}^{\text{II}}\text{-sq})$ / E_h	Complexes	$E(\text{LS-Co}^{\text{III}}\text{-cat})$ / E_h	$E(\text{HS-Co}^{\text{II}}\text{-sq})$ / E_h
1	-2994.831976	-2994.825854	24	-3336.678671	-3336.691588
2	-3034.160841	-3034.161159	25	-3073.489425	-3073.493211
3	-3073.487493	-3073.493996	26	-3148.510721	-3148.511390
4	-3112.810997	-3112.825457	27	-3302.192006	-3302.197136
5	-4636.649328	-4636.653788	28	-3455.865574	-3455.880483
6	-13092.06922	-13092.07407	29	-3302.175931	-3302.167905
7	-4518.667034	-4518.654734	30	-3455.855282	-3455.846607
8	-4557.995440	-4557.989127	31	-2686.287252	-2686.287152
9	-4597.322735	-4597.321948	32	-2922.244248	-2922.251091
10	-12974.07303	-12974.05942	33	-2843.523005	-2843.541807
11	-13013.40250	-13013.39400	34	-2919.791345	-2919.792510
12	-13052.72898	-13052.72705	35	-3077.094587	-3077.096379
13	-2680.245771	-2680.237354	36	-2998.440408	-2998.441991
14	-2719.574481	-2719.569981	37	-12516.66185	-12516.65867
15	-2758.900021	-2758.903407	38	-3051.395370	-3051.393601
16	-2798.223647	-2798.235302	39	-3107.957482	-3107.963757
17	-2837.536911	-2837.531525	40	-3164.520148	-3164.531335
18	-2876.865556	-2876.864171	41	-3068.657484	-3068.659275
19	-2916.191510	-2916.198068	42	-4592.495112	-4592.491573
20	-2955.515203	-2955.529787	43	-2792.630323	-2792.623807
21	-3218.698981	-3218.692772	44	-4366.194148	-4366.184864
22	-3258.032565	-3258.035488	45	-2833.924571	-2833.912847
23	-3297.351530	-3297.358788			

4. Effect of Redox-Active vs Ancillary Ligand.

While many factors can influence the VT process, the coordination environment of the molecule plays a crucial role in determining whether a molecule will display VT or likely remain in its temperature-invariant forms. In general, the ancillary ligands sterically modulate the redox-potential of the Co^{II}/Co^{III} redox couple while the substitution in the redox-active ligands contributes the tuning of $cat^{2-}/ sq^{\bullet-}$ redox potential.[39] Steric crowding in the coordination environment, imparted from ancillary ligands, can cause an increase in metal-ligand bond lengths to stabilise the HS-Co^{II}-sq form. Consequently, those with high steric crowding will have smaller ΔE_{Gas} values and are likely to be in the HS-Co^{II}-sq form. Conversely, if the coordination sphere is less crowded, the molecule will tend to adopt smaller metal-ligand bond lengths / molecular volume and will stabilise the LS-Co^{III}-cat form. As a result, the ΔE_{Gas} values will be larger (and positive) and will likely be in their LS-Co^{III}-cat form.

On the other hand, the electron-withdrawing/donating nature of substituents on the redox-active ligand can modulate the electronic properties, with increased electron withdrawing stabilising the LS-Co^{III}-cat, resulting an increase in the ΔE_{Gas}. Therefore, the redox-potentials of the metal-ligand pair, serving as a proxy for the energies of the orbitals that participate in the VT electron transfer, need to be compatible to achieve VT.

The family of [Co(Xdiox)(Me$_n$tpa)]$^+$ complexes exemplifies this effect. As illustrated in **Fig. 2**, valence tautomerism is observed for Me$_2$tpa with electron donating groups on the Xdiox (**3**, **23**, **25**) and for Me$_3$tpa with electron withdrawing groups on the Xdiox (**5** and **6**). Reducing the number of methyl groups on the Me$_n$tpa ligand ($n = 0, 1$) reduces the steric hindrance and causes stabilisation of LS-Co^{III}-cat form with all Xdiox ligands (**1**, **2**, **21**, **45**). With electron donating Xdiox ligands, the use of Me$_3$tpa stabilises HS-Co^{II}-sq (**4**, **24**). Given this qualitative argument, we

sought to elucidate the relative contributions of the ancillary and the redox-active ligands. We have utilised the [Co(Xdiox)(Me$_n$tpa)]$^+$ family of complexes including the hypothetical analogues, for its gradual tunability. (**Table S12**) Previous DFT-based analysis of [Co(Xdiox)(Me$_n$tpa)]$^+$ has shown minimal effects for the different structural isomers that arise from Me$_n$tpa coordination,[24] reducing the complexity of the analysis.

Table S12. Relative valence tautomer energies for the series of [Co(Xdiox)(Me$_n$tpa)]$^+$ complexes calculated with M06L-D4/def2-TZVPP method in gas phase to explore steric vs electronic effects in the family of Me$_n$tpa.

Increasing steric

Dioxolene ligand	ΔE_{Gas} / kJ mol^{-1} of [Co(Xdiox)(Me$_n$tpa)]$^+$				
	$n = 0$	$n = 1$	$n = 2$	$n = 3$	
Br$_4$diox	35.7^a	22.3^a	5.1^a	-12.7^b	
Cl$_4$diox	32.3^{a*}	16.6^a	2.1^a	-11.7^b	Increase
H$_4$diox	22.1^a	11.8^a	-8.9^b	-30.6^c	electron
4-tbdiox	14.1^a	3.6^a	-17.2^b	-38.3^c	donation
3,5-dbdiox	16.1^{a*}	-0.8^{a*}	-17.1^{b*}	-38.0^{c*}	

^{a} LS-Co^{III}-(cat) complexes (blue); ^{b} VT complexes (green) including predicted; ^{c} VT complexes (red).

*Reported complexes

The calculations indicate that increased steric crowding imparted by the ancillary ligands and enhanced electron donation in the redox-active ligands results in decreased ΔE_{Gas} values, favouring the HS-Co^{II}-sq form. However, it is evident that both effects exert differing degrees of influence on the ΔE_{Gas} values. The slight modification of the electron donating/withdrawing capability of substituents on the dioxolene ligands, (i.e. Br$_4$diox to Cl$_4$diox; or 4-tbdiox to 3,5-dbdiox) corresponds to a change of only ~ 0.1 – 5.7 kJ mol^{-1}, while adding one methyl group to the pyridine rings of the ancillary ligand (i.e $n = 0$ to $n = 1$) contributed to an energy change of

~10.3 – 22.4 kJ mol^{-1}. Therefore, the experimental observation of gaining or losing VT with increasing number of methyl substituents in this family of complexes can be unambiguously rationalised. To surpass this energy change in the ancillary ligand, the dioxolene ligand needs to be significantly modified (from electron donating to electron withdrawing groups) to retain VT. Therefore, it is clear from the analysis that the steric effects from the ancillary ligands dominate over electronic effects from the redox-active ligands in the Me$_n$tpa family. This behaviour is also observed throughout all the families (cyclams, pyrazoles, quinolines and azamacrocycles) of monocationic complexes.

5. Structural Data and Description

Yellow green single crystals of formula [C$_{26}$H$_{26}$N$_4$O$_2$Co][BPh$_4$] (**15.BPh$_4$)** were crystallised by layering DCM/hexane solutions. Two crystallographically independent molecules were found in the asymmetric unit, which crystallised in the non-centrosymmetric space group Pna2$_1$. In one cation the two methyl groups of the ligand were localised, while the other had one of the methyl groups distributed over two positions with occupancy factors of 0.65:0.35 (slight variation with temperature) . This difference between almost equivalent cations leads to a lowering of the crystal symmetry, resulting in a non-centrosymmetric space group. The crystal was also racemicially twinned, the twin components refined to 0.6:0.4 (slight variation with temperature).

Dark Purple single crystals of formula [C$_{30}$H$_{34}$N$_4$O$_2$Co][BPh$_4$] (**19.BPh$_4$)** were crystallised by layering DCM solution with hexane. The crystal appeared to show minor translational disorder (by about -0.01, 0.05, -0.02). As this component was small (<10%) attempts to model this disorder were not successful. The maximum and minimum electron density peaks were 2.14 and -1.20 eÅ^{-3} close to the Co atom, attributable to this disorder. The two methyl groups on the pyridine rings of

the ligand were distributed over the three possible pyridine rings, the final occupancy factors were 0.859(3):0.629(3):0.512(3) (for 100K, slight variation for other temperatures). Attempts to model the excess electron density near the Co atom were unsuccessful.

Green single crystals of formula $[C_{28}H_{30}N_4O_2Co][BPh_4].0.75(CH_2Cl_2)$ (**17.BPh$_4$·0.75DCM**) were crystallised by layering DCM solution with hexane. There are molecules of DCM in the asymmetric unit. One molecule was fully occupied while the other was only partly occupied, the occupancy factor of the latter refined to a value close to 0.5; for convenience the occupancy factor was fixed at 0.5. The crystal was solved and refined in the space group $P2_1$, as a racemic twin with ratio 0.60(2):0.40(2). The possibility of the space group being $P2_1$/c, rather than twinned $P2_1$ was investigated. Although a solution was possible in $P2_1$/c, there were a large number of reflections that should have been systematically absent but were not, many with I > 15 sig(I). The Rint value was higher (6.15%) and the R-value did not refine to below 10.24%. Accordingly, the refinement was continued in the space group $P2_1$, as a 2-component inversion twin with two cations, two anions, one fully occupied molecule of dichloromethane and one molecule of dichloromethane which was 50% occupied. The *tert*-butyldioxolene ligands showed signs of disorder. Attempts to model this were not successful. The final difference map showed electron density peaks close to the Cobalt atoms and the *tert*-butyl groups. There were a number of solvent voids in the structure; none contained any solvent and so refinement was continued without the application of the OLEX2 solvent mask routine. In all cases, crystals were directly transferred from mother liquor to the crystal oil to avoid any loss of solvents or crystallinity.

Further details for each structure at each temperature are available in the deposited CIFs.

Table S13. Variable temperature crystallographic data for compound **15.BPh₄**

	100 K	150 K	200 K	270 K	330 K	370 K
formula	$C_{50}H_{46}BCoN_4O_2$	$C_{50}H_{46}BCoN_4O_2$	$C_{50}H_{46}BCoN_4O_2$	$C_{50}H_{46}BCoN_4O_2$	$C_{50}H_{46}BCoN_4O_2$	$C_{50}H_{46}BCoN_4O_2$
fw/g mol^{-1}	804.65	804.65	804.65	804.65	804.65	804.65
T/K	99.96(2)	150.12(2)	201.34(2)	270.15	330.0(2)	371.6(2)
crystal syst.	orthorhombic	orthorhombic	orthorhombic	orthorhombic	orthorhombic	orthorhombic
space group	$Pna2_1$	$Pna2_1$	$Pna2_1$	$Pna2_1$	$Pna2_1$	$Pna2_1$
a/Å	29.620(6)	29.670(6)	29.760(6)	29.872(6)	30.000(6)	30.090(6)
b/Å	9.840(2)	9.860(2)	9.890(2)	9.931(2)	9.980(2)	10.040(2)
c/Å	27.530(6)	27.580(6)	27.660(6)	27.754(6)	27.840(6)	27.930(6)
α/deg	90	90	90	90	90	90
β/deg	90	90	90	90	90	90
γ/deg	90	90	90	90	90	90
V/Å^3	8024(3)	8068(3)	8141(3)	8233(3)	8335(3)	8438(3)
Z	8	8	8	8	8	8
ρ_{calc} g/cm3	1.332	1.325	1.313	1.298	1.282	1.267
μ/mm^{-1}	0.475	0.472	0.468	0.463	0.457	0.452
reflns measd	153146	154621	154945	96159	159410	164000
unique reflns	19719	19869	19993	19053	20601	20703
R$_{int}$	0.0776	0.0739	0.0670	0.0394	0.0310	0.0396
data/restraints/param	19719/2/1061	19869/2/1062	19993/2/1055	19053/11/1062	20601/2/1061	20703/2/1061
GOF on F^2	1.029	1.016	1.011	1.082	1.008	0.979
R_1 [I>2σ (I)]	0.0513	0.0482	0.0478	0.0456	0.0404	0.0470
wR_2	0.1427	0.1289	0.1330	0.1505	0.1280	0.1622
$\Delta\rho_{max/min}$/ e Å^{-3}	0.71/-0.39	0.38/-0.39	0.23/-0.50	0.42/-0.54	0.23/-0.24	0.28/-0.12

Table S14. Variable temperature crystallographic data for compound **19.BPh$_4$**

	100 K	150 K	200 K	250 K	275 K	300K	325 K	350 K	375 K	400 K
formula	$C_{54}H_{54}BCoN_4O_2$	$C_{54}H_{54}BCoN_4O_2$	$C_{54}H_{54}BCoN_4O_2$	$C_{54}H_{54}BCoN_4O_2$	$C_{54}H_{54}BCoN_4O_2$	$C_{54}H_{54}BCoN_4O_2$	$C_{54}H_{54}BCoN_4O_2$	$C_{54}H_{54}BCoN_4O_2$	$C_{54}H_{54}BCoN_4O_2$	$C_{54}H_{54}BCoN_4O_2$
fw/g mol^{-1}	860.75	860.75	860.75	860.75	860.75	860.75	860.75	860.75	860.75	860.75
T/K	100.0(2)	153.0(2)	202.0(2)	252.0(2)	276.0(2)	302.0(2)	327.0(2)	352.0(2)	376.0(2)	400.0(2)
crystal syst.	monoclinic	monoclinic	monoclinic	monoclinic	monoclinic	monoclinic	monoclinic	monoclinic	monoclinic	monoclinic
space group	$P2_1/n$	$P2_1/n$	$P2_1/n$	$P2_1/n$	$P2_1/n$	$P2_1/n$	$P2_1/n$	$P2_1/n$	$P2_1/n$	$P2_1/n$
a/Å	20.212(4)	20.258(4)	20.325(4)	20.402(4)	20.464(4)	20.525(4)	20.581(4)	20.625(4)	20.675(4)	20.716(4)
b/Å	9.6340(19)	9.6480(19)	9.6710(19)	9.6920(19)	9.7080(19)	9.7270(19)	9.7470(19)	9.765(2)	9.779(2)	9.795(2)
c/Å	22.929(5)	22.962(5)	23.011(5)	23.077(5)	23.147(5)	23.244(5)	23.342(5)	23.419(5)	23.468(5)	23.515(5)
α/deg	90	90	90	90	90	90	90	90	90	90
β/deg	95.57(3)	95.60(3)	95.61(3)	95.63(3)	95.64(3)	95.61(3)	95.56(3)	95.51(3)	95.49(3)	95.47(3)
γ/deg	90	90	90	90	90	90	90	90	90	90
V/Å^3	4443.7(15)	4466.5(16)	4501.4(16)	4541.2(16)	4576.3(16)	4618.4(16)	4660.4(16)	4694.9(17)	4723.0(17)	4749.8(17)
Z	4	4	4	4	4	4	4	4	4	4
ρ_{calc} g/cm3	1.287	1.280	1.270	1.259	1.249	1.238	1.227	1.218	1.210	1.204
μ/mm^{-1}	0.433	0.431	0.428	0.424	0.421	0.417	0.413	0.410	0.408	0.405
reflns measd	81287	81606	82140	83080	83740	84382	85136	85992	86768	86859
unique reflns	13279	13327	13432	13560	13668	13760	13826	13891	13954	13963
R_{int}	0.0520	0.0594	0.0713	0.0595	0.0539	0.0551	0.0571	0.0636	0.0674	0.0589
data/restraints/param	13279/1/578	13327/1/578	13432/1/578	13560/1/578	13668/1/578	13760/1/578	13826/1/578	13891/1/578	13954/1/578	13963/1/578
GOF on F^2	1.046	1.054	1.026	1.035	1.057	1.060	1.069	1.051	1.067	1.066
R_1 [$I>2\sigma (I)$]	0.0676	0.0680	0.0742	0.0769	0.0783	0.0757	0.0724	0.0709	0.0699	0.0624
wR_2	0.1815	0.1883	0.2055	0.2210	0.2341	0.2356	0.2354	0.2327	0.2405	0.2157
$\Delta\rho_{max/min}$/ e Å^{-3}	2.13/-1.20	2.31/-1.30	2.57/-1.35	2.42/-1.41	2.03/-1.32	1.46/-1.03	1.07/-0.72	0.93/-0.55	0.78/-0.56	0.58/-0.41

Table S15. crystallographic data for compound **17.BPh₄·0.75DCM** at 100 K

	17.BPh₄·0.75DCM
formula	$C_{105.5}H_{103}B_2Cl_3Co_2N_8O_4$
fw/g mol^{-1}	1792.78
T/K	100.0(2)
crystal syst.	monoclinic
space group	$P2_1$
a/Å	14.769(3)
b/Å	15.187(3)
c/Å	21.191(4)
α/deg	90
β/deg	106.73(3)
γ/deg	90
V/Å^3	4551.9(17)
Z	2
ρ_{calc} g/cm3	1.308
μ/mm^{-1}	0.511
reflns measd	80343
unique reflns	26377
R$_{int}$	0.0574
data/restraints/param	26377/15/1141
GOF on F^2	1.063
R_1 [I>2σ (I)]	R1 = 0.0716, wR2 = 0.2093
wR_2	R1 = 0.0917, wR2 = 0.2286
$\Delta\rho_{max/min}$/ e Å^{-3}	0.99/-0.67
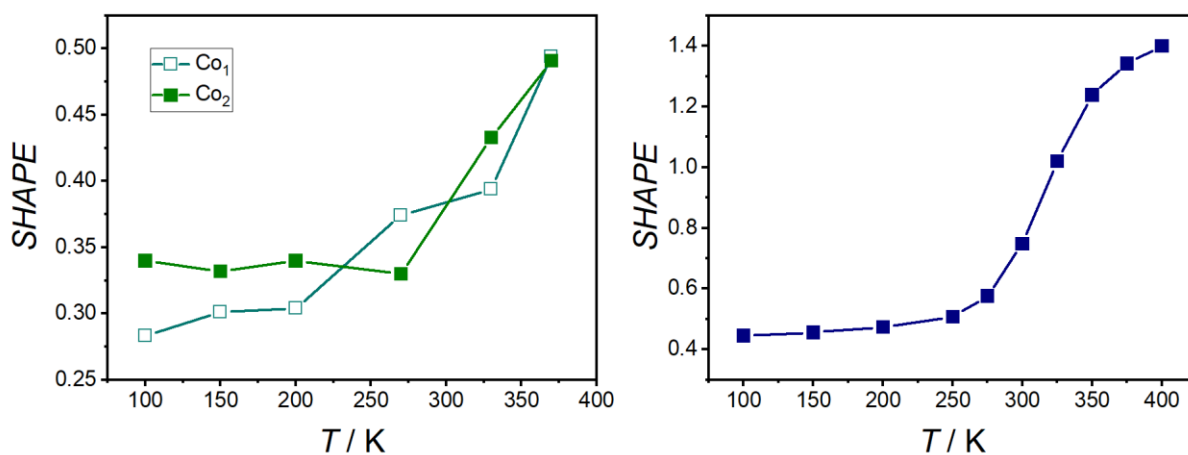
Fig. S9 Temperature dependence of octahedral *SHAPE* index for complex **15.BPh₄** (left) and for the two crystallographic independent molecules in compound **19.BPh₄** (right)
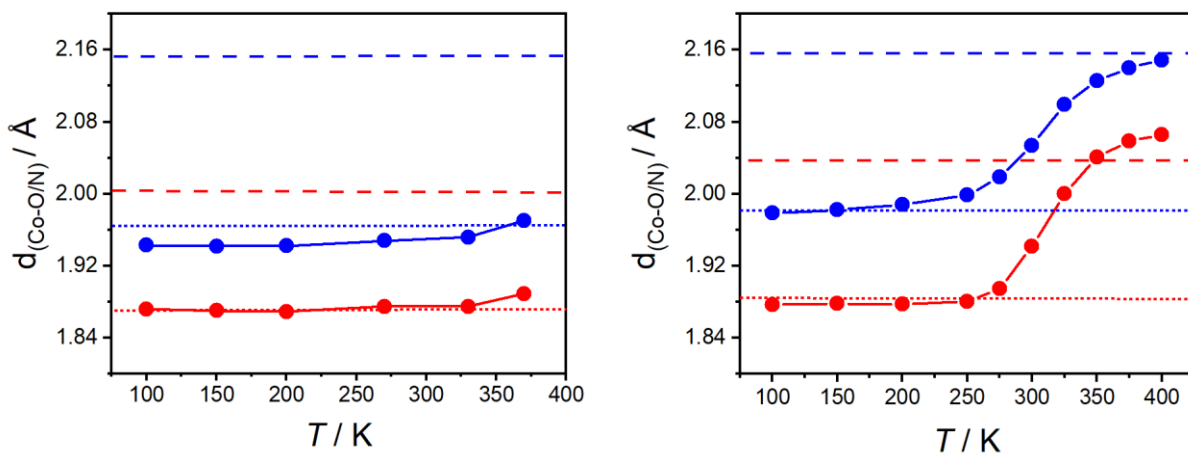
Fig. S10 Temperature dependence of average Co–O (Red) and average Co–N (Blue) bond lengths of **15.BPh₄** (left) and **19.BPh₄** (right) from single crystal XRD measurements in comparison to average Co–O and Co–N bond lengths calculated for LS-Co^{III}-cat (dotted) and HS-Co^{II}-sq (dashed) from DFT geometry optimisation with BP86-D3(BJ)/def2-TZVP in gas phase.
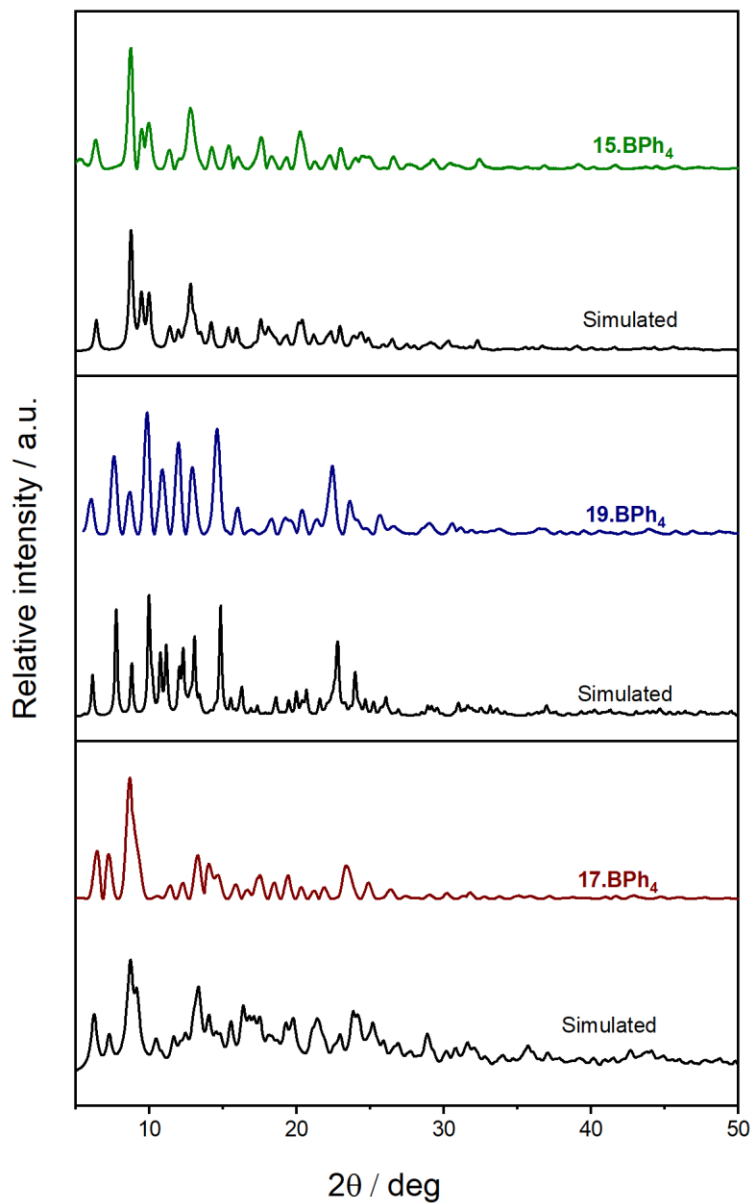
Fig. S11 Experimental PXRD pattern for **15.BPh₄** (green), **19.BPh₄** (blue) and **17.BPh₄** (red) with their respective simulated PXRD (black) from crystal structures of **15, 19** and **17** at 100 K. The difference in intensities for simulated vs experimental pattern is attributed to preferred orientation.

6. Thermogravimetric Analysis (TGA)
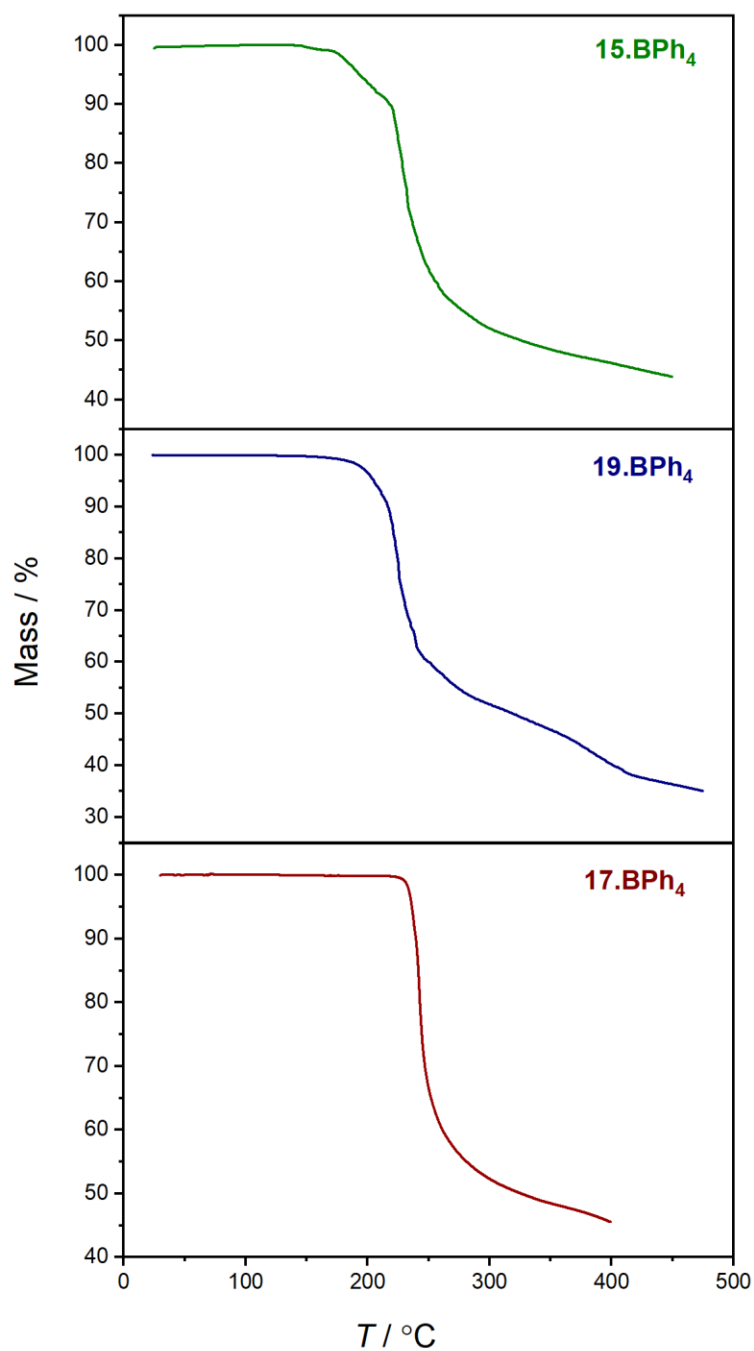
Fig. S12 Thermogravimetric analysis profile for complex **15.BPh₄** (top) and **19.BPh₄** (middle) and **17.BPh₄** (bottom) at a ramp rate of 5 °C/min, indicating no solvents in the bulk compounds.

7. Infrared Spectroscopy
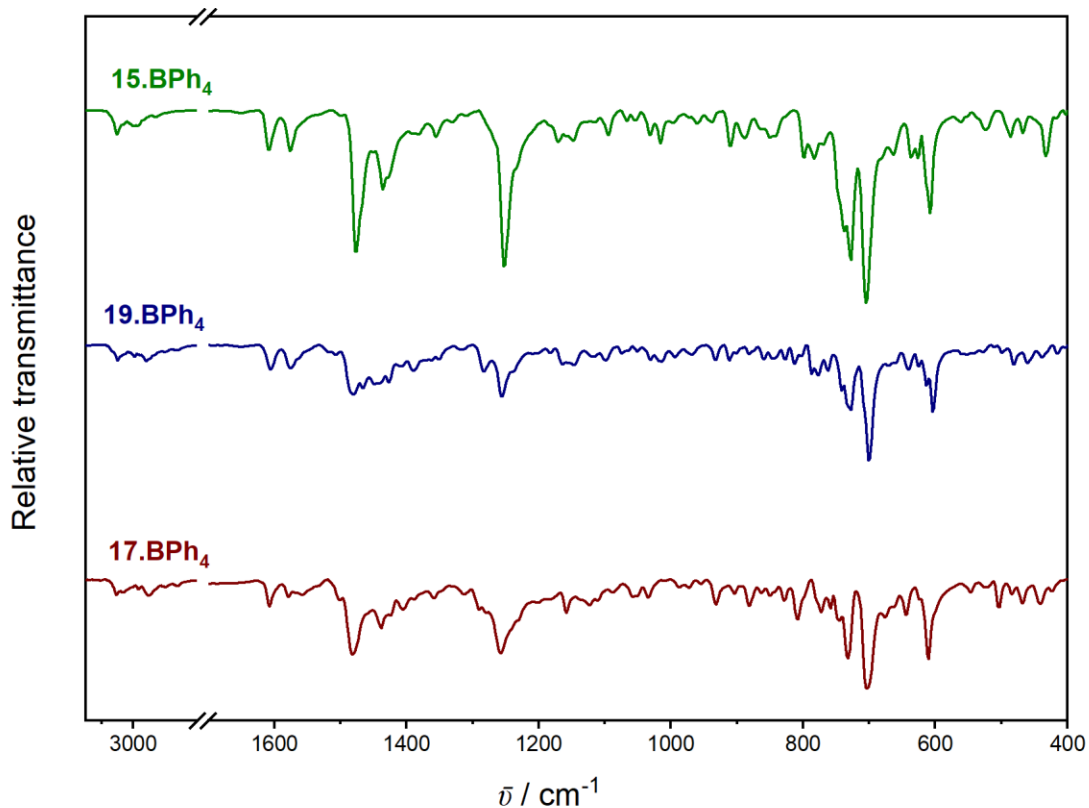
Fig. S13 ATR-IR spectra of complexes **15.BPh₄** (green), **19.BPh₄** (blue) and **17.BPh₄** (red).

Table S16. Selected IR bands (cm^{-1}) assignments of complexes **15.BPh₄**, **19.BPh₄** and **17.BPh₄**

Moiety / functional groups	Wavenumber ($\bar{v}$) / cm^{-1}			Ref
	15.BPh₄	**19.BPh₄**	**17.BPh₄**	
tpa	1609, 1576	1607, 1576	1607, 1578	40,41
tert-butyl	-	2957, 2864, 1283	2954, 2864, 1285	42
sq•⁻	-	1451, 1514	-	40,41,43
cat²⁻	1228, 1355, 1436	-	1228, 1357, 1438	24,40,41,43
BPh₄⁻	702, 607	700, 603	700, 609	24
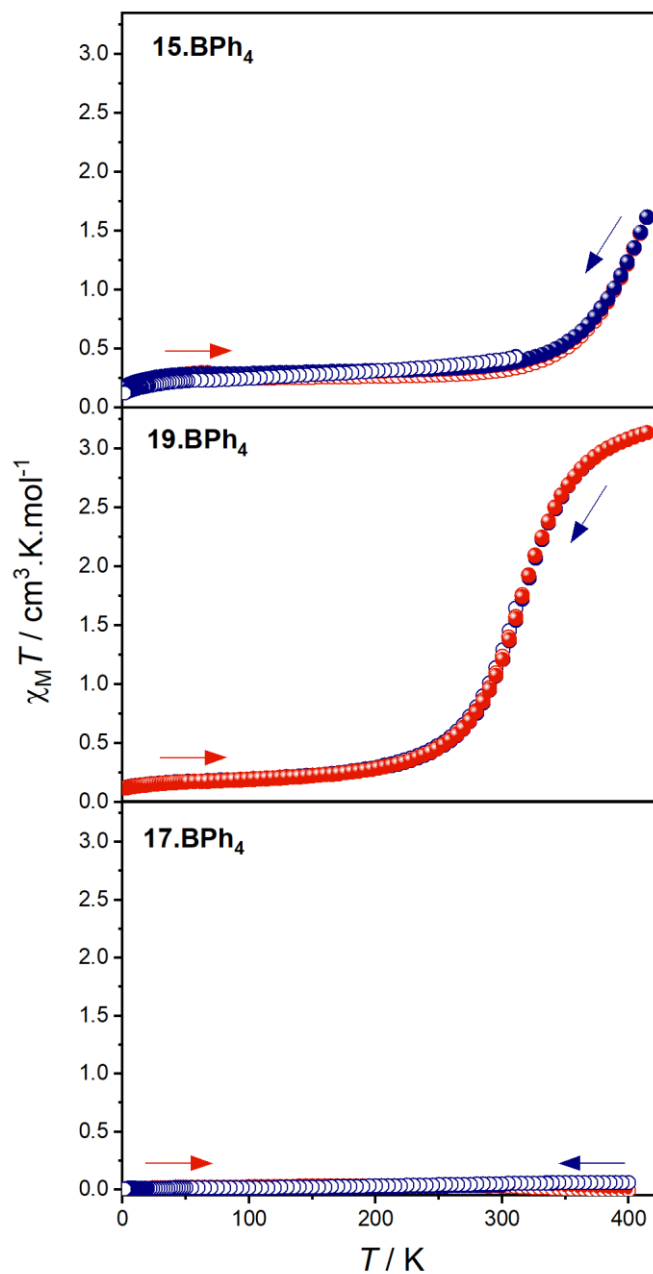
Fig. S14 Plot of $\chi_M T$ vs T for solid-state **15.BPh₄** (top), **19.BPh₄** (middle) and **17.BPh₄** (bottom) on the order of first cooling 300–1.8 K (blue open circles), first heating 1.8–400 K (red open circles), second cooling 400–1.8 K (blue spheres) and second heating 1.8 K–300 K (red spheres). Red and blue arrows indicate heating and cooling directions respectively.

8. Electronic Absorption Spectroscopy

The spectral features are generally characteristic to the tautomeric form. Complex **15** displays interesting behaviour in different solvents at room temperature. In MeCN, the dissolved complex of **15** was greenish-yellow and exhibits a broad peak at ~670 nm and ~390 nm, characteristic to a LS-Co^{III}-cat species.[1,24,44] The complex dissolved in chlorinated solvents DCE and DCM was greenish blue, with an intense band at ~420 nm and two broad peaks at ~590 nm and ~670 nm, inherent to a HS-Co^{II}-sq species. The colour of the solution in acetone and BuCN were green, and the recorded spectra lies in between the two extremes with a broad peak at ~670 nm and a shoulder at ~590 nm, suggestive of an intermediate electronic state. However, complex **19**, in all solvents displays similar spectral features with an intense band at ~410 nm, a broad peak at ~570 nm and a shoulder at ~660 nm, typical to a HS-Co^{II}-sq electronic state (**Fig. S15**). UV-vis spectra recorded for **17** in all solvents had a broad peak around ~700 nm and an intense band at ~380 nm, with no peaks appearing at 500–600 nm, is similar to that of **15** in MeCN, indicating a LS-Co^{III}-cat species (**Fig. S15**).
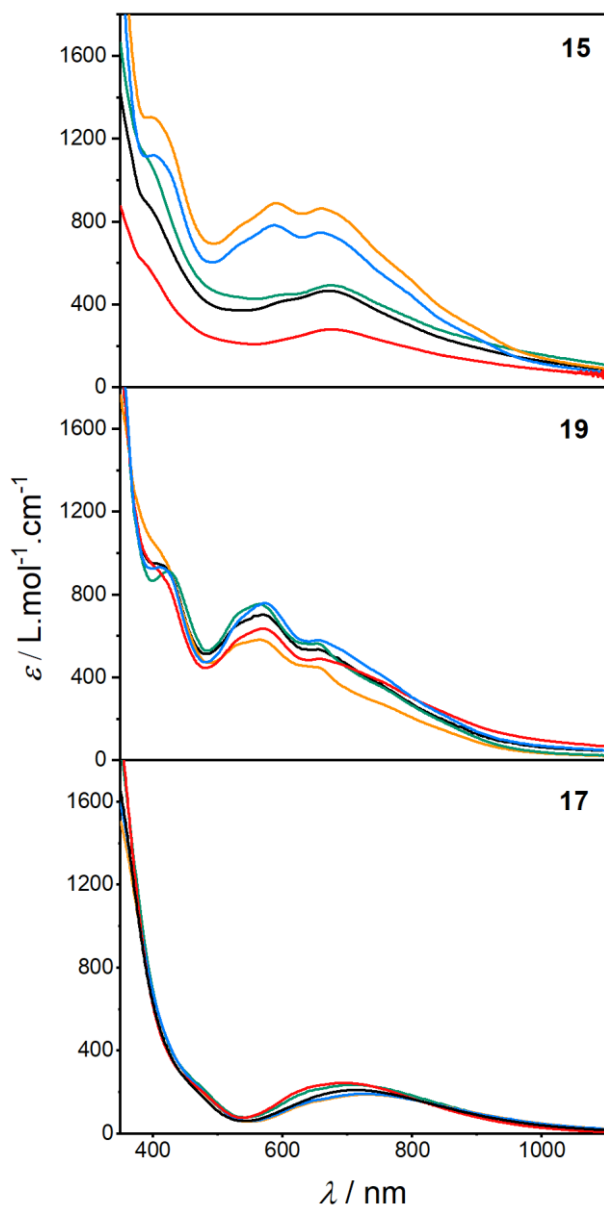
Fig. S15 Electronic absorption spectroscopy of complexes **15** (top) and **19** (middle) and **17** (bottom) in DCE (orange), DCM (blue), acetone (green), BuCN (black) and MeCN (red).

The high intense absorptions occurring in blue region (380–420 nm) could be attributed to a ligand-to-metal charge transfer (LMCT) in LS-Co^{III}-cat form (cat^{2-} to the LS-Co^{III} e$_g$*) and metal-to-ligand charge transfer (MLCT) in HS-Co^{II}-sq form (HS-Co^{II} eg* to sq•− π*). The latter is observed to increase with temperature, forming the first isosbestic/near isosbestic point. This is apparent from both experimental,[1,24,44] and TD-DFT studies performed previously by us on Co-dioxolene complexes.[1] The second prominent feature observed at ~590 and ~570 nm for **15** and **19** respectively, is too intense for a d–d transition and therefore assigned as the $^4T_{1g} \rightarrow$ $^4T_{1g}$ (P) transitions,[45] characteristic to *pseudo*-octahedral HS-Co^{II} ion. The second possibility for such species is $^4T_{1g} \rightarrow$ $^4A_{2g}$, which is often obscured by the high intensity of the former band.[44,45] This is further reinforced by bleaching of the band with decreasing temperature upon formation of the LS-Co^{III} ion for both **15** and **19 (Fig. S20–S21)**. It is worth noting that this band (570–590 nm) is absent for **17,** a pure LS-Co^{III}-cat component, which is existent for **19** in all solvents and for **15** in DCE and DCM at room temperature (**Fig. S15**). As such this band appears highly specific to the HS-Co^{II}-sq species as observed for other analogues.[24,40,44,46,47] Additionally, the broad peak emerging at 660–670 nm for all the complexes regardless of the tautomeric-state, is assigned to internal ligand charge transfer transition.[43,44,48] This transition originating from π → π* orbitals of the dioxolene ligand, becomes more prominent for sq•−,[1] with increasing temperature. With the absence of the band at 570–590 nm, the former band (660–670 nm) appears to be notable in the LS-Co^{III}-cat state, forming a distinct spectrum as seen in **17** for all solvents and **15** in MeCN, BuCN and acetone (**Fig. S15**). This spectral feature is also observed with metal-dioxolene complexes other than cobalt,[46,48] confirming the origin of transition being ligand-based. With the observed variation in spectral transitions across different solvents, a salient feature to note is that

the stability of each tautomeric form is highly modulated by solvents similar to that of the effect of temperature.

Table S17. Prominent electronic absorption bands observed for complexes **15, 19** and **17** in various solvents in UV-vis absorption spectroscopy at 298 K, and their corresponding band assignments.

Solvent	Observed band at 298 K / nm			Assignment	Ref
	15	**19**	**17**		
MeCN	~670 (broad)	~570 (broad)	~690 (broad)	660 -710 nm:	[1,44,45]
	~390 (intense)	~ 660 (sh)	~ 380 (intense)	Internal ligand transfer	
		~ 420 (intense)		(sq$^{\bullet-}$ $\pi \rightarrow \pi^*$)	
Acetone	~670 (broad)	~570 (broad)	~690 (broad)	570 -590 nm:	[24,45]
	~590 (sh)	~ 660 (sh)	~ 380 (intense)	$^4T_{1g} \rightarrow {}^4T_{1g}$ (P)	
	~390 (intense)	~ 420 (intense)			
BuCN	~670 (broad)	~~570 (broad)	~700 (broad)	380 nm:	[1]
	~590 (sh)	~ 660 (sh)	~ 380 (intense)	LMCT	
	~390 (intense)	~ 420 (intense)		(cat^{2-} $\rightarrow$ LS-Co^{III} eg*)	
DCM	~670 (broad)	~570 (broad)	~710 (broad)	420 nm:	[1,24]
	~590 (broad)	~ 660 (sh)	~ 380 (intense)	MLCT	
	~420 (intense)	~ 420 (intense)		(HS-Co^{II} eg* $\rightarrow$ sq$^{\bullet-}$ π^*)	
DCE	~670 (broad)	~570 (broad)	~710 (broad)		
	~590 (broad)	~ 660 (sh)	~ 380 (intense)		
	~420 (intense)	~ 420 (intense)			

sh -refers to shoulder
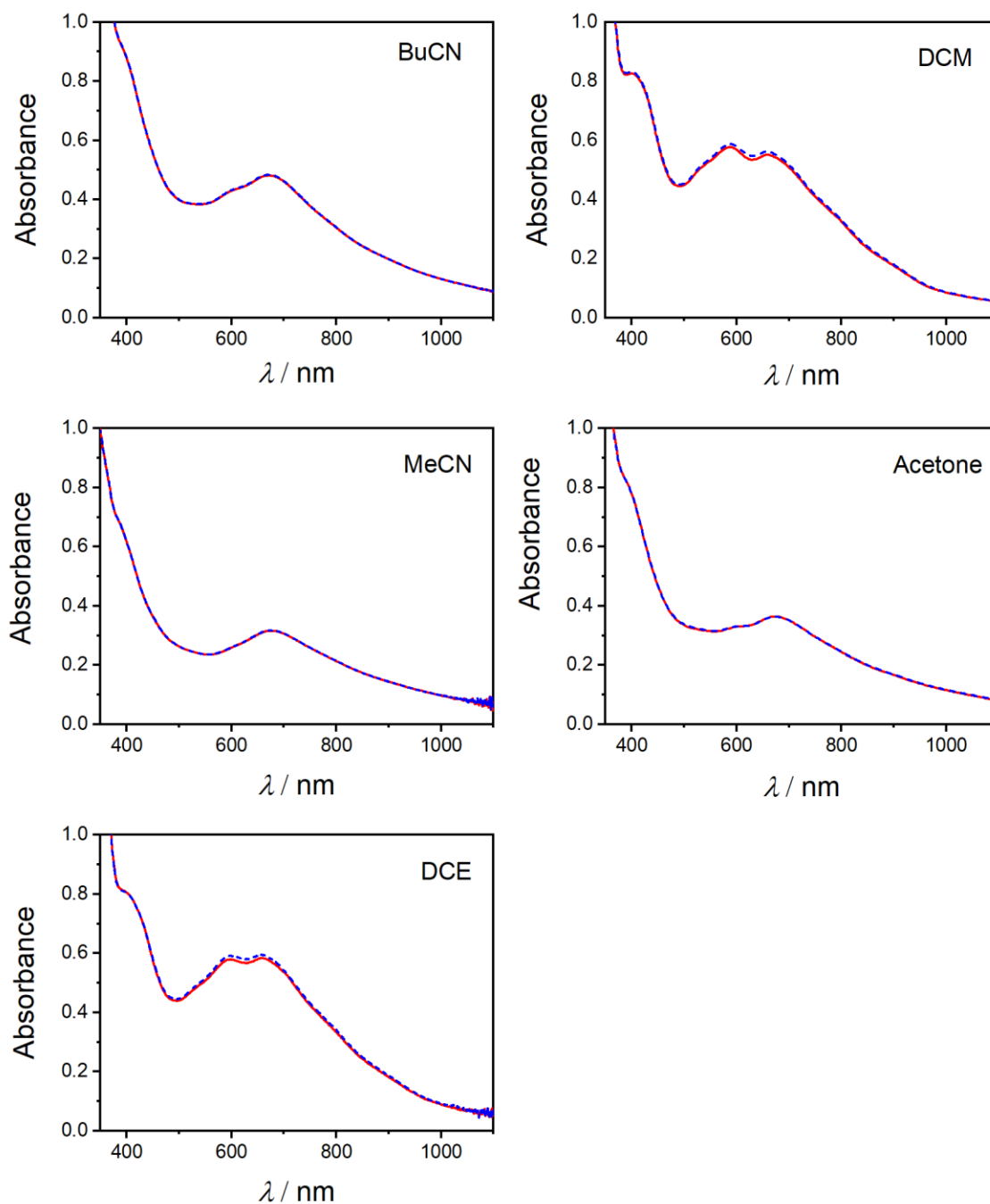
Fig. S16 UV-vis absorption spectra of **15** in various solvents under aerobic conditions immediately after dissolution (red solid line) and after 2–3 hours (blue dashed line).
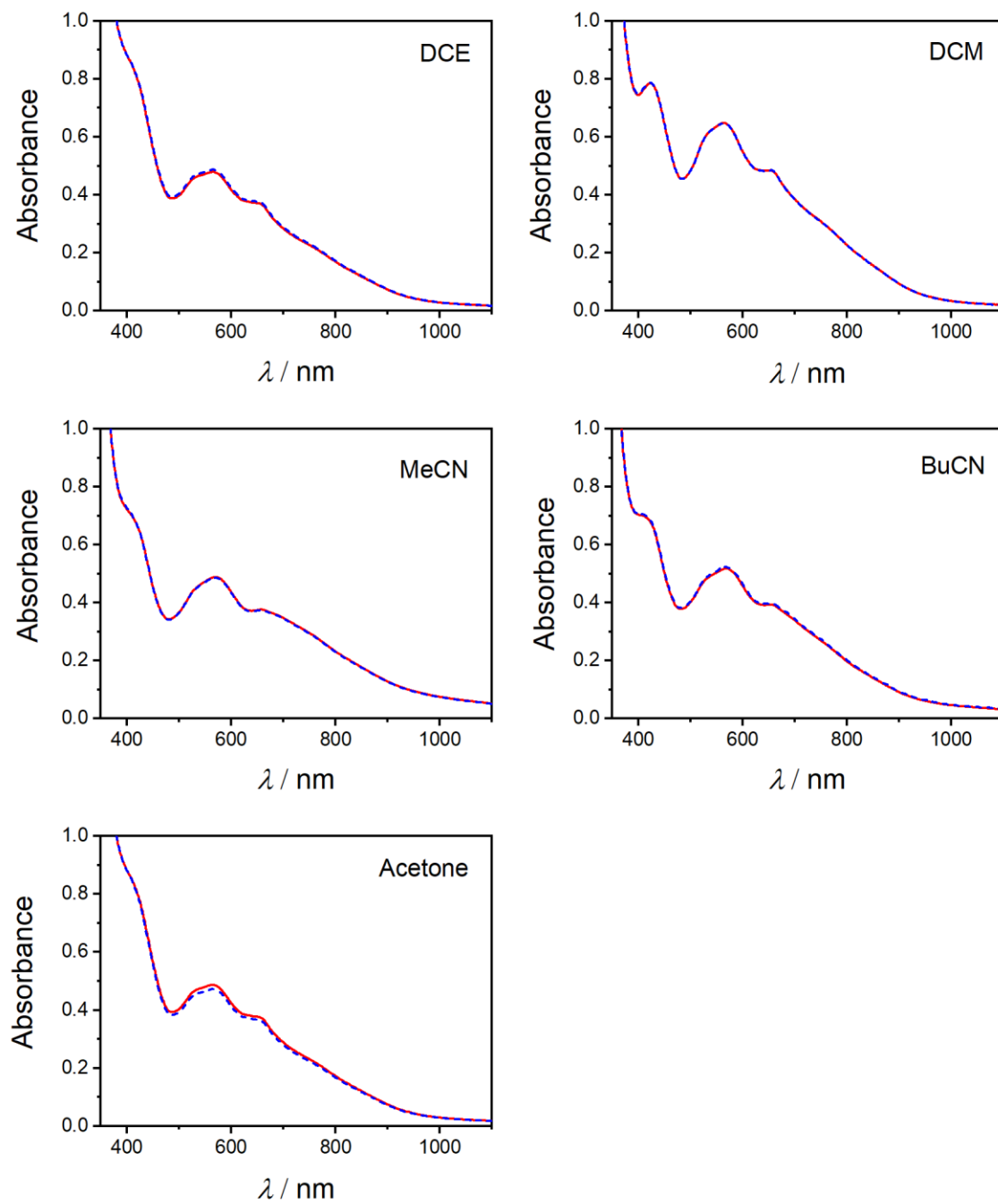
Fig. S17 UV-vis absorption spectra of **19** in various solvents under aerobic conditions immediately after dissolution (red solid line) and after 3–4 hours (blue dashed line).
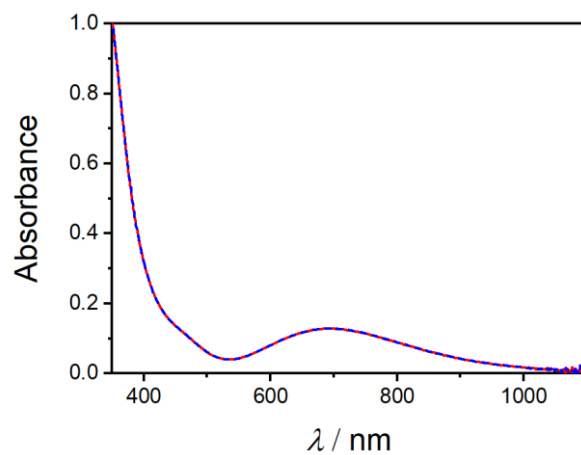
Fig. S18 UV-vis absorption spectra of **17** in MeCN under aerobic conditions immediately after dissolution (red solid line) and after 4 hours (blue dashed line).

Variable Temperature Electronic Absorption Spectroscopy
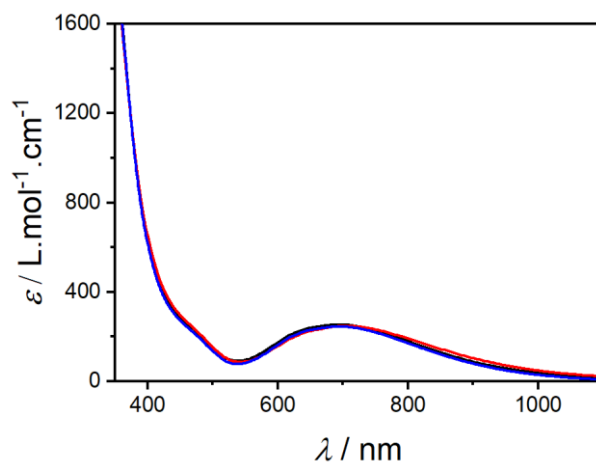
Fig. S19 UV-vis absorption spectra of **17** in MeCN at 298 K immediately after dissolution (black solid line) and after heating up to 333 K (red line); indicative of no VT transition.
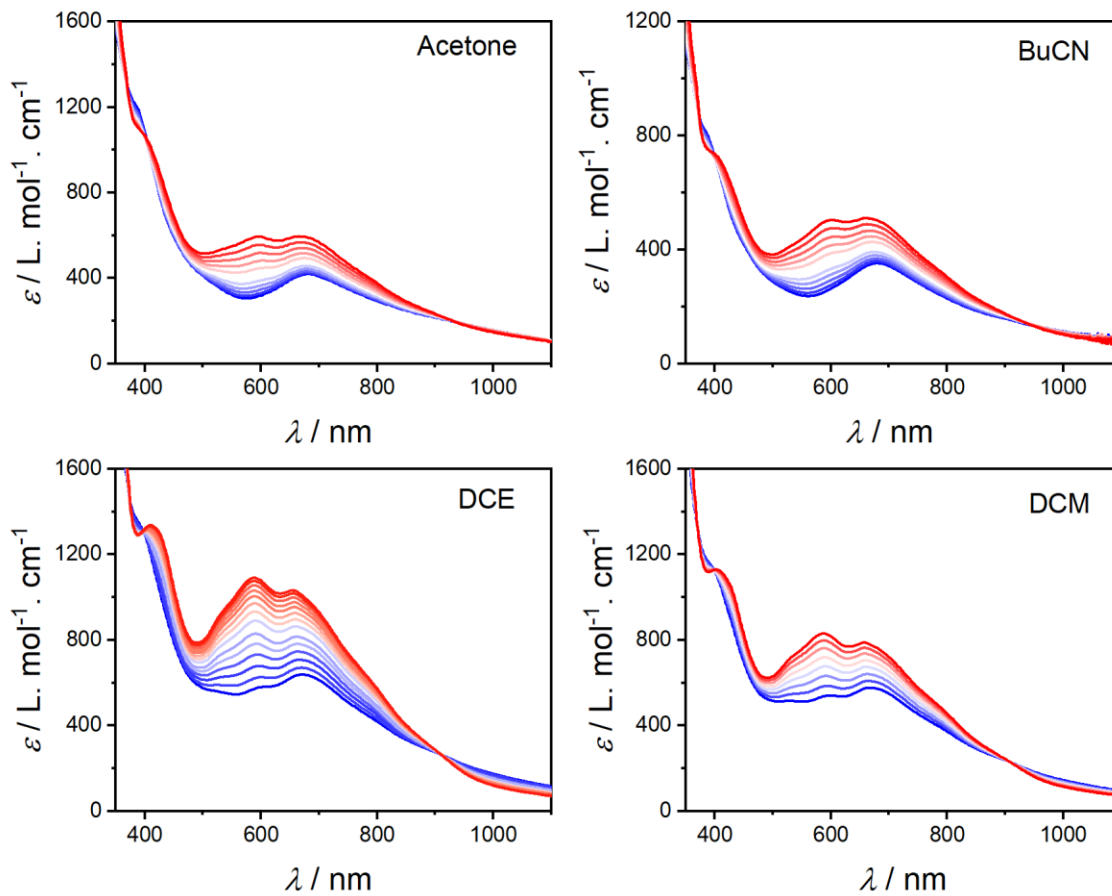
Fig. S20 Variable temperature UV-vis absorption spectra of **15** in MeCN (268–328 K), BuCN (268–318 K), acetone (268–318 K), DCM (268–303 K) and DCE (268–323 K) with 5 K intervals.
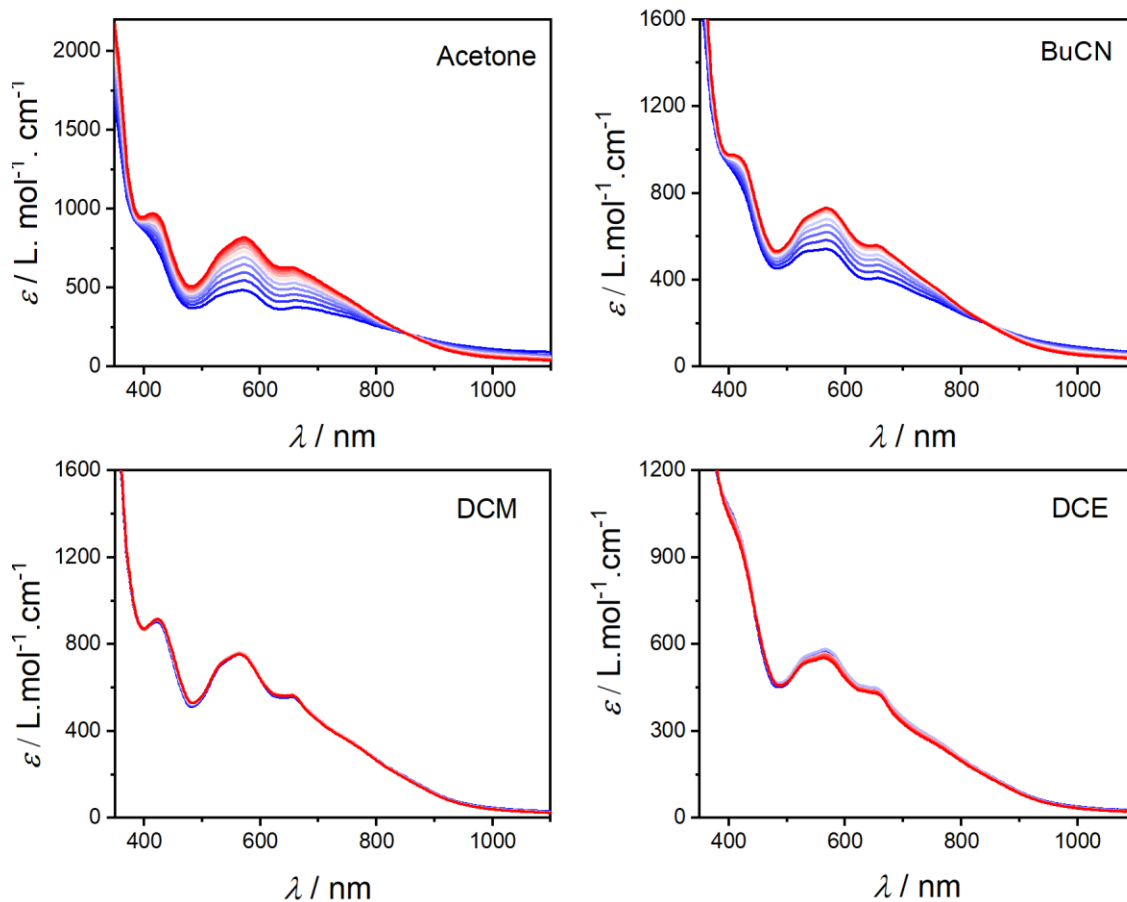
Fig. S21 Variable temperature UV-vis absorption spectra of **19** in MeCN (268–343 K), BuCN (268–318 K), acetone (268–318 K), DCM (268–298 K) and DCE (268–318 K) with 5 K intervals. (The change in spectra for DCE and DCM is not visible in the recorded temperature range)

9. Electrochemistry

Cyclic voltammetry (CV) and steady-state rotating disk electrode (RDE) were used to study the electrochemical properties of **15, 17** and **19**. The mid-point potentials (E_m) of each compound reported in **Table S18** was calculated by taking the average of the cathodic peak potential (E_{pc}) and anodic peak potentials (E_{pa}) of each process from the cyclic voltammograms. Where possible peak-to-peak separations (ΔE_p) are also given.
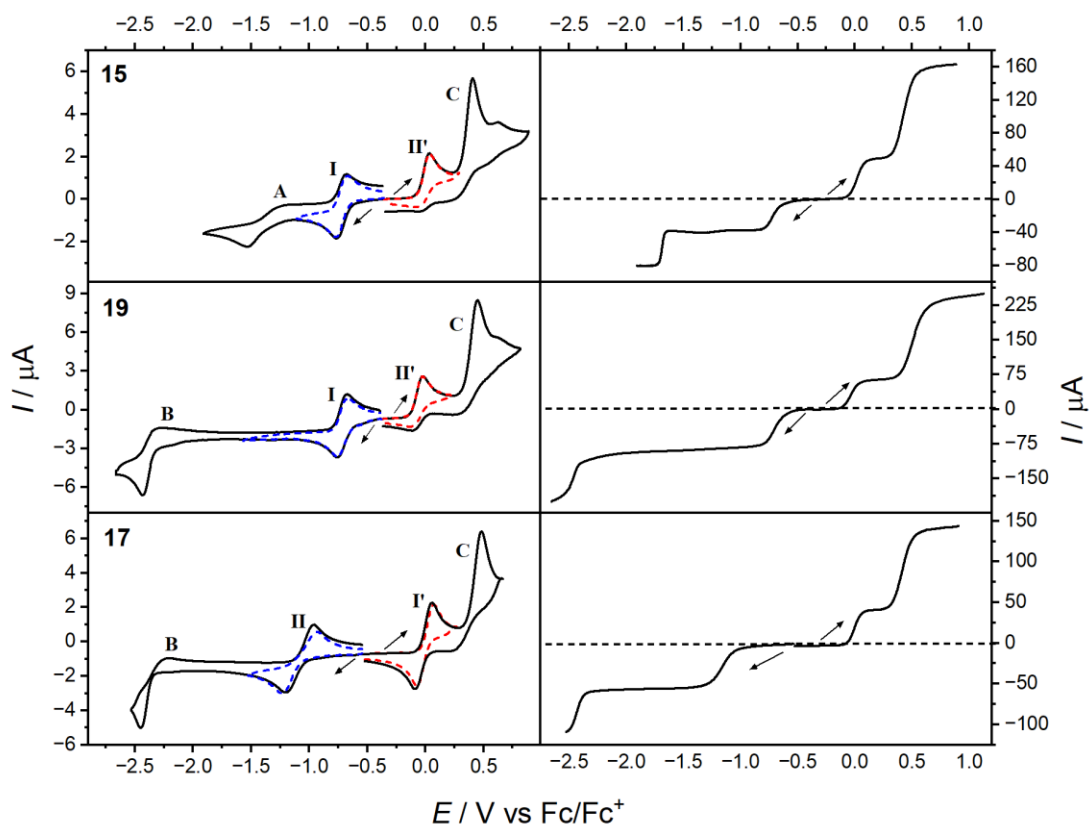
Fig. S22 Cyclic (100 mV/s) (left) and rotating disk electrode (1000 rpm) (right) voltammograms in MeCN (1.0 mM with 0.1 M BuN$_4$PF$_6$) for **15** (top), **19** (middle) and **17** (bottom). The blue and red lines plot the voltammograms with an immediate switching potential past the first reduction and first oxidation respectively. Arrows indicate the directions of the scan.

Complexes **15**, **19** and **17** display two resolved reduction processes (**I/II** and **A/B**) and two well distinguished oxidation processes (**I'/II'** and **C**) in the accessible potential window, which are reinforced by the position of the zero current in the RDE voltammograms. Cyclic voltammograms suggest that process **I** and **II'** of **15** and **19** are electrochemically reversible/quasi-reversible (ΔE_p below 85 mV), whilst **17** all the processes appear to be irreversible. Limiting currents of RDE voltammograms of all three complexes indicate that all are one electron (1e⁻) processes except for process **C**.

It is apparent from the electronic absorption spectroscopy that **17** is observed as pure LS-Co[III]-cat component in MeCN. Therefore, the 1st reduction process of **17** (process **II**) ($E_m = -1.09$ V) can be assigned as a metal-based reduction of Co(III) to Co(II) and the 1st oxidation process (process **I**, -0.016 V) is ligand based, from cat²⁻ to sq•⁻. Complexes **15** and **19** exist as a mixture of both LS-Co[III]-cat and HS-Co[II]-sq in MeCN at ambient conditions (**Fig. 5**, See VT UV-vis spectroscopy section) with the HS-Co[II]-sq form predominating. It is apparent from the RDE and cyclic voltammograms that the first oxidation and first reductions for **15** and **19** are similar in potential and reversibility. The 1st oxidation (process **II'**) is assigned as a cobalt oxidation, whilst the 1st reduction (process **I'**) is the semiquinonate reduction. It is typical for this family of complexes that the dioxolene process exhibits a greater degree of reversibility than the Co(III)/Co(II) process, as is observed here for all three complexes.[40,46]

Process **A** of **15** occurs at -1.405 V and is not observed for **19** and **17**. It is known that absorbed hydrogen on the electrode can cause multi-stepped reactions in catechol, which is further influenced by the acidity of the solvent and the substitutions in the catechol itself.[49] This process might thus be due to the reduction of Hcat⁻ to dianion and hydrogen. This observation is consistent with a previous observation of an analogous process for isolated catechol and that is absent with

3,5-di-*tert*-butylcatechol in MeCN.[49] However, process **B** of **19** and **17** occurring at more negative potentials, originating from tpa is in accordant with similar analogues.[24,40] Analogous with previous cases, process **C** of all three complexes are irreversible and result from oxidation of tetraphenylborate counterions,[46] the RDE limiting currents suggestive of a two-electron oxidation.

The difference in the mid-point potentials of the 1st oxidation process and the 1st reduction process (where one process is metal-based and the other being ligand-based) can be defined as $\Delta ox\text{-}red$.[24,40] For cobalt-dioxolene complexes, where $\Delta ox\text{-}red$ < 740 mV, a thermally-induced VT transition can typically be accessed.[24,40] The calculated $\Delta ox\text{-}red$ value for **15** and **19** are 721 mV and 659 mV respectively, consistent with the observed thermally accessible VT transitions. The $\Delta ox\text{-}red$ value determined for **17** is 1073 mV, indicative of the processes being significantly separated and confirming the incapability for VT.

Table S18. Cyclic voltammetry data for complexes **15**, **19** and **17** in MeCN (0.1 M BuN$_4$PF$_6$) solutions.

Process	15		19		17	
	*E_p or E_m/V,	(ΔE_p/mV)	E_p or E_m/V,)	(ΔE_p/mV	E_p or E_m/V,	(ΔE_p/mV)
A	-1.405	271	-	-	-	-
B	-	-	-2.366	149	-2.334	216
I / I'	-0.728	88	-0.709	73	-0.015	145
II / II'	-0.006	73	-0.050	73	-1.088	236
C	0.407	-	0.470	-	0.480	-
$\Delta ox\text{-}red$	721 mV		659 mV		1073 mV	

*E_m is provided whenever possible, and for highly irreversible processes for which an E_{pc} or E_{pa} is not clearly observed the prominent peak position is considered.

Table S19. Assignments of each process for cyclic voltametric data for complexes **15**, **19** and **17**

Process	15	19	17	Ref
A (1e⁻)	$Hcat + e^- \rightleftharpoons Hcat^{2-} \cdot \rightleftharpoons 1/2H_2 + cat^{2-}$		-	[49]
B (1e⁻)	-	$Me_n tpa$ based reductions		[24]
I/I' (1e⁻)		$sq^{\bullet-} + e^- \rightleftharpoons cat^{2-}$		[24,40,43,46]
II/II' (1e⁻)		$Co^{3+} + e^- \rightleftharpoons Co^{2+}$		[24,40,43,46]
C (2e⁻)		$BPh_4^- \rightleftharpoons BPh_2^+ + Ph\text{–}Ph + 2e^-$		[12,46]

10. Solution Magnetic Measurements
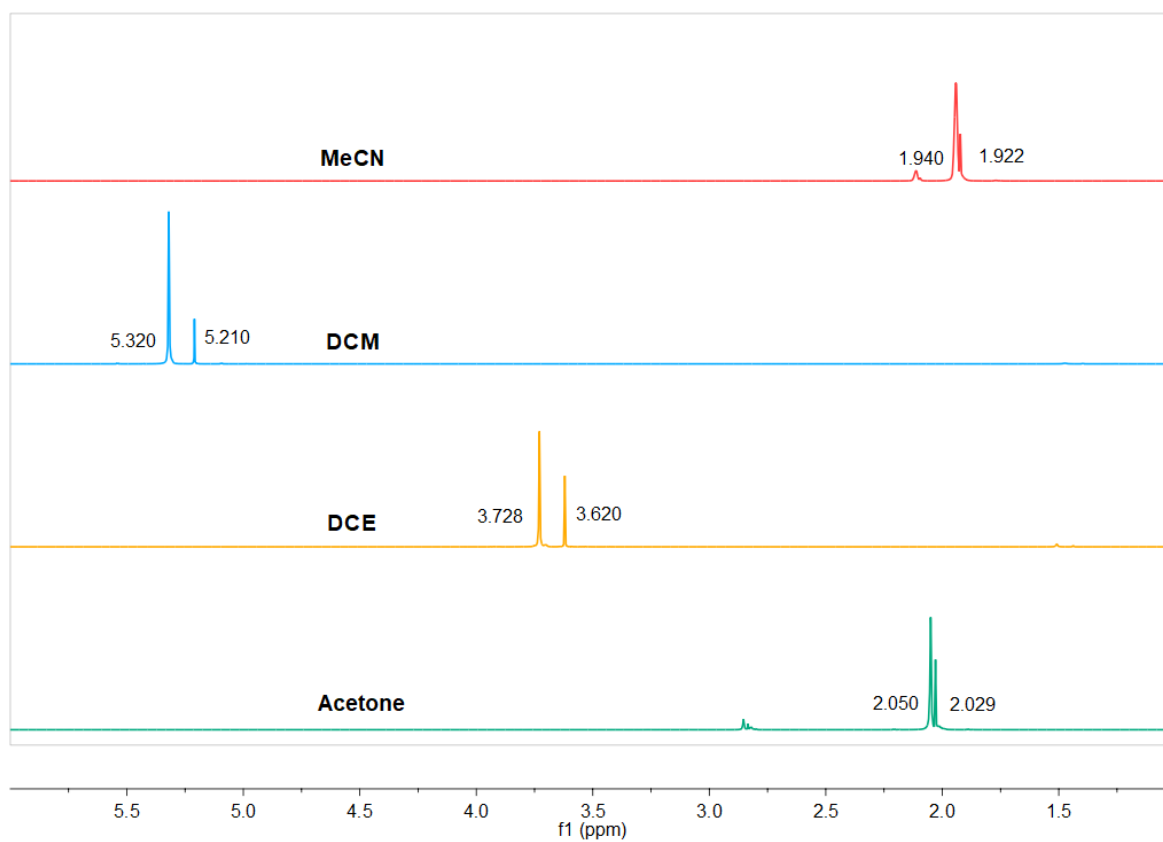
Fig. S23 ^{1}H NMR obtained for **15** at 298 K representing inner and outer peak shifts in MeCN (red), DCM (blue), DCE (yellow) and acetone (green).
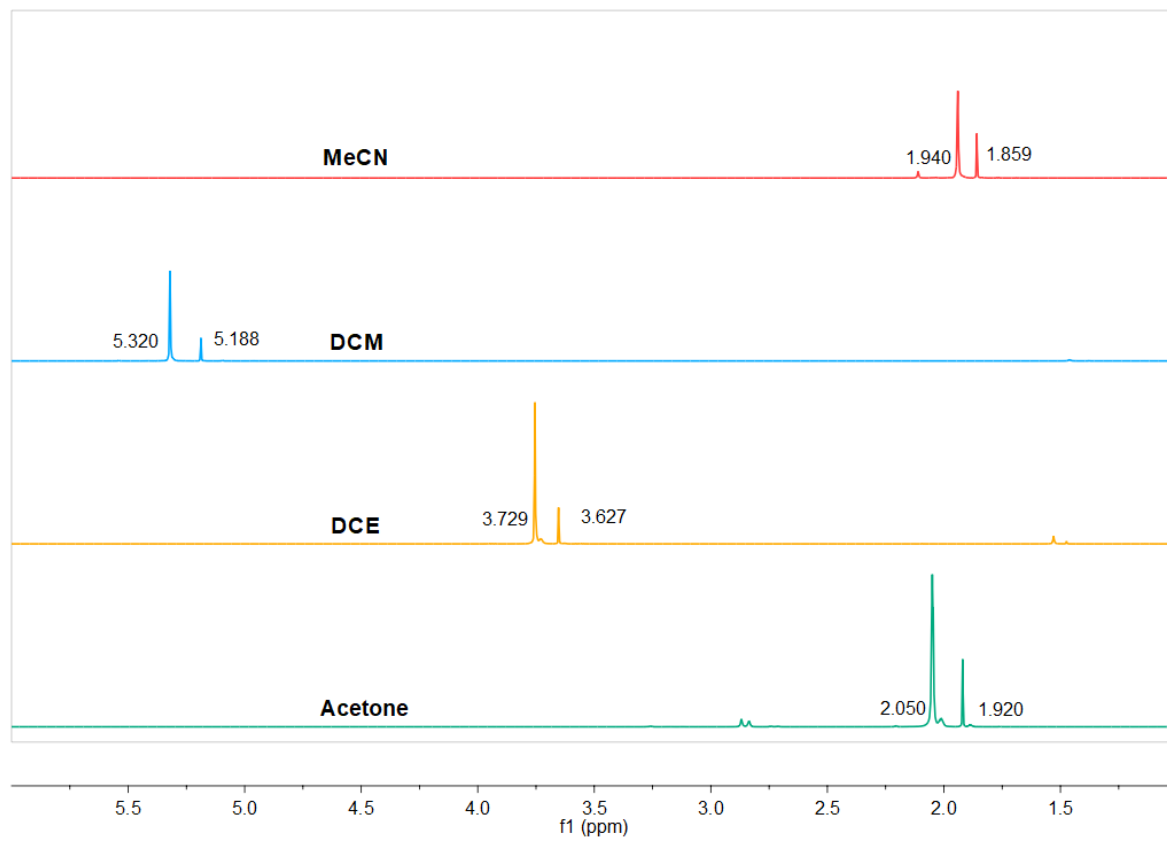
Fig. S24 ^{1}H NMR obtained for **19** at 298 K representing inner and outer peak shifts in MeCN (red), DCM (blue), DCE (yellow) and acetone (green).
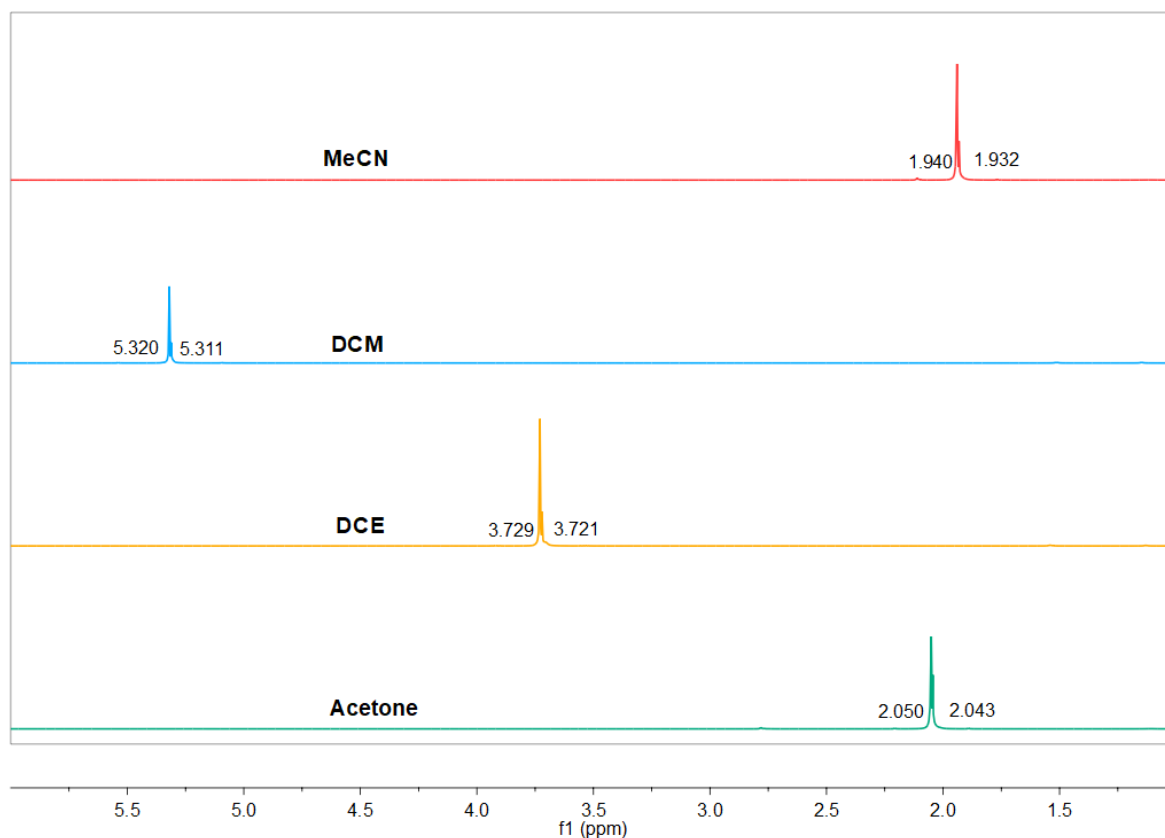
Fig. S25 ^{1}H NMR obtained for **17** at 298 K representing inner (reference) and outer (sample) peak shifts in MeCN (red), DCM (blue), DCE (yellow) and acetone (green).

Table S20. The $\chi_M T$ values determined at 298 K for complexes **15**, **19** and **17** in various solvents.

Solvent	$\chi_M T$ in solution/ cm^3 K mol^{-1}		
	15	**19**	**17**
MeCN	0.44	1.94	0.28
DCM	1.79	3.35	0.31
DCE	1.67	3.18	0.29
Acetone	0.45	2.61	0.25

The solution magnetic measurements obtained at 298 K for **15, 17** and **19** are in accordance with the tautomeric state at room temperature established by electronic absorption spectroscopy. Complex **15** showed smaller peak separations in acetone and MeCN giving $\chi_M T$ values of ~0.4 cm^3 K mol^{-1}, indicative of a LS-Co^{III}-cat form. Whilst in DCM and DCE **15** had a larger separation with a $\chi_M T$ values centred around 1.7 cm^3 K mol^{-1} suggesting towards a HS-Co^{II}-sq form. Measurements for **19** at 298 K in all the solvents had well shifted peaks with comparatively larger $\chi_M T$ values (1.9–3.3 cm^3 K mol^{-1}), suggestive of a HS-Co^{II}-sq from. For **17,** the peak separations at 298 K were minimal in all the solvents measured and the $\chi_M T$ values determined were < 0.3 cm^3 K mol^{-1} indicating a pure LS-Co^{III}-cat form.

11. $T_{1/2}$ Correlations and Thermodynamic Parameters

Table S21. Calculated ΔE_S and $\Delta E_S + \Delta E_{Gas}$ and experimentally reported $T_{1/2}$ for complex **6** ([Co(Br$_4$diox)(Me$_3$tpa)]$^+$) in various solvents. (In ref. 24)

Solvent	ΔE_S / kJ mol^{-1}	$\Delta E_S + \Delta E_{Gas}$ / kJ mol^{-1}	$T_{1/2}$ / K
MeCN	36.7	24.0	359
DCM	32.4	19.7	291
DCE	33.1	20.4	295

ΔE_S and $\Delta E_S + \Delta E_{Gas}$ are calculated with M06L-D4/def2-TZVPP as $E_{HS-CoII-sq} - E_{LS-CoIII-cat.}$
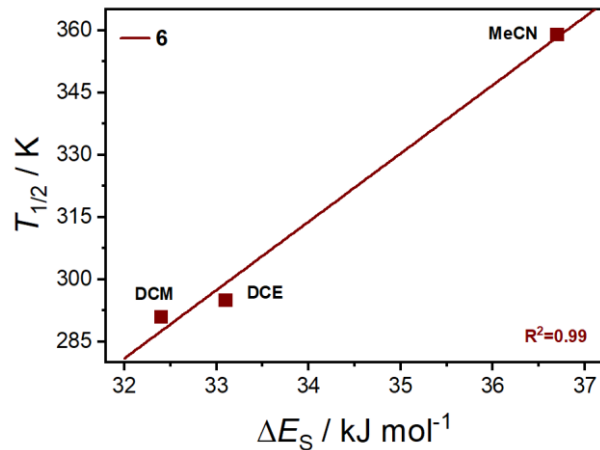
Fig. S26 Correlation of the experimentally determined $T_{1/2}$ values for complex **6** in various solvents reported in ref. 24 with respective calculated ΔE_S. (Calculations performed with M06L-D4/def2-TZVPP).
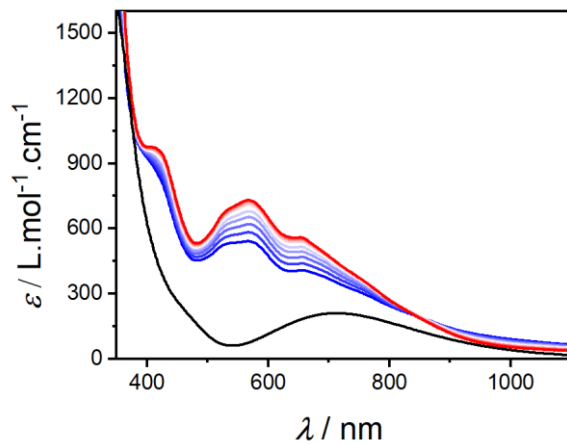
Fig. S27 Variable temperature UV-vis absorption spectra of **19** in BuCN (Red to blue represents 318 K to 268 K with 5 K intervals) and spectrum of **17** in BuCN at 298 K (Black).

Complex **17**, the tpa analogue of **19,** is experimentally verified to be in the LS-Co$^{\text{III}}$-cat form. Therefore, the spectrum of **17** in BuCN is assumed to be the analogous 100% LS-Co$^{\text{III}}$-cat spectrum of **19**. The 318 K spectrum of **19** in BuCN, that outreach saturation, is set as 100% HS-Co$^{\text{II}}$-sq component. Using the two spectra as limiting compositional references, a spectral deconvolution has been performed for each spectrum (between 380–1100 nm range) to determine the HS-Co$^{\text{II}}$-sq composition at each temperature. The plot of %HS-Co$^{\text{II}}$-sq composition with temperature fitted to the regular solution model, appears to follow a sigmoidal curve (**Fig. S28**). Thermodynamic parameters extracted from the plot gives an estimated $T_{1/2}$ of 261 ± 7 K.
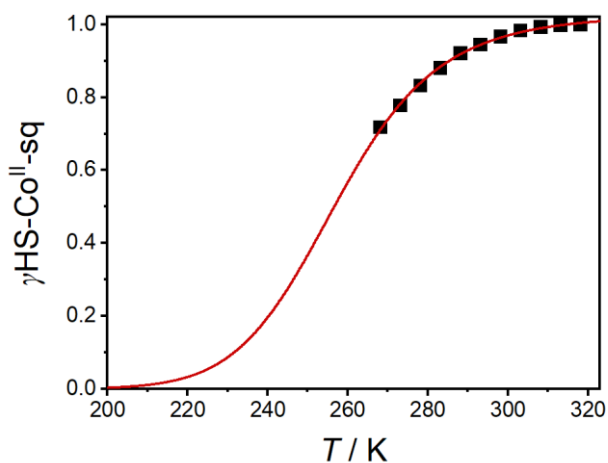
Fig. S28 Temperature dependence of the molar fraction of HS-Co$^{\text{II}}$-sq tautomer in **19** (BuCN) (■), fit with regular solution model (red line) (R^2 = 1.00).

Chart S1. Neutral family of [Co(3,5-dbdiox)(3,5-dbsq)(N₂L)] complexes
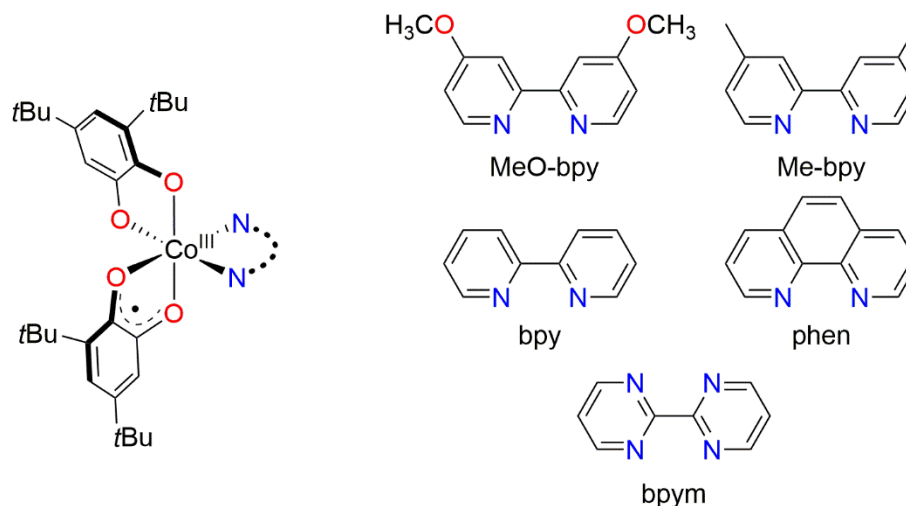
Table S22. Calculated ΔE_{Gas}, ΔE_S and $\Delta E_S + \Delta E_{Gas}$ and experimentally reported $T_{1/2}$ for [Co(3,5-dbdiox)(3,5-dbsq)(N₂L)] family of complexes in toluene.

Complex[a,b,*]		$\Delta E_{Gas}{}^c$ / kJ mol⁻¹	$\Delta E_S{}^c$ (Toluene) / kJ mol⁻¹	$\Delta E_S + \Delta E_{Gas}$ / kJ mol⁻¹	$T_{1/2}{}^d$ / K	Ref
[Co(3,5-dbdiox)(3,5-dbsq)(phen)]	**46⁰**	15.8	4.2	20.0	227	50
[Co(3,5-dbdiox)(3,5-dbsq)(bpy)]	**47⁰**	21.7	4.2	25.9	277	50
[Co(3,5-dbdiox)(3,5-dbsq)(Me-bpy)]	**48⁰**	22.9	4.4	27.3	287	50
[Co(3,5-dbdiox)(3,5-dbsq)(MeO-bpy)]	**49⁰**	26.1	4.7	30.8	336	1
[Co(3,5-dbdiox)(3,5-dbsq)(bpym)]	**50⁰**	18.6	1.8	20.4	190	51

[a] The abbreviations of the ligands stands for, MeO-bpy = 4,4′-dimethoxy-2,2′-bipyridine; bpy = 2,2′-bipyridine; phen = 1,10′-phenanthroline, Me-bpy = 4,4′-dimethyl-2,2′-bipyridine; bpym = 2,2′-bipyrimidine [b] Geometry optimisations performed with PBEh-3c. [c] ΔE_S and ΔE_S are calculated with M06L-D4/def2-TZVPP as $E_{HS\text{-}CoII\text{-}sq} - E_{LS\text{-}CoIII\text{-}cat.}$ *Complexes with 2,2′-bipyrazine (bpyz) for which a $T_{1/2}$ is not known and 4,4′-diphenyl-2,2′-bipyridine (ph-bpy) which is a known anomaly are excepted.

12. Energy and Dipole Moment

Table S23. Individual dipole moment of the complexes calculated with M06L-D4/def2-TZVPP in MeCN and in gas phase.

Complexes	μ(LS-Co^{III}-cat) / Debye (MeCN)	μ(HS-Co^{II}-sq) / Debye (MeCN)	μ(LS-Co^{III}-cat) / Debye (Gas)	μ(HS-Co^{II}-sq) / Debye (Gas)	$\Delta\mu${(HS-Co^{II}-sq) – (LS-Co^{III}-cat)} / Debye	
					MeCN	Gas
3	19.78	13.07	13.34	8.60	-6.71	-4.74
5	25.97	19.69	18.58	13.72	-6.28	-4.86
6	30.03	23.83	22.24	17.54	-6.20	-4.70
15	16.12	9.82	10.36	5.88	-6.30	-4.48
19	18.73	11.83	12.76	7.75	-6.90	-5.01
27	20.15	13.98	13.38	8.78	-6.17	-4.60
32	20.39	13.35	13.32	7.82	-7.04	-5.51
35	20.66	16.05	13.35	10.54	-4.61	-2.81
41	20.26	14.10	17.51	13.29	-6.16	-4.22
46^0	13.04	10.17	9.81	8.23	-2.87	-1.58
47^0	12.56	9.74	9.45	7.88	-2.82	-1.57

Table S24. Total electronic energies of the complexes calculated with M06L-D4/def2-TZVPP in gas phase and in MeCN.

Complexes	E_{Gas} (LS-Co^{III}-cat) / E_h	E_{Gas} (HS-Co^{II}-sq) / E_h	E_S (LS-Co^{III}-cat) / E_h (MeCN)	E_S (HS-Co^{II}-sq) / E_h (MeCN)
3	-3073.487493	-3073.493996	-3073.560813	-3073.555901
5	-4636.649328	-4636.653788	-4636.731043	-4636.722285
6	-13092.06922	-13092.07407	-13092.15052	-13092.14147
15	-2758.900021	-2758.903407	-2758.975594	-2758.967311
19	-2916.191510	-2916.198068	-2916.266207	-2916.261132
27	-3302.192006	-3302.197136	-3302.266664	-3302.259656
35	-3077.094587	-3077.096379	-3077.169362	-3077.161719
32	-2922.244248	-2922.251091	-2922.331122	-2922.322343
41	-3068.657484	-3068.659275	-3068.740709	-3068.729819
46^0	-3346.976203	-3346.970189	-3347.004722	-3346.995556
47^0	-3270.728606	-3270.720339	-3270.757299	-3270.745846

Table S25. Individual dipole moment of the complexes calculated with M06L-D4/def2-TZVPP in different solvents for complexes **15** and **19**.

Solvent	15			19		
	μ(LS-Co^{III}-cat) / Debye	μ(HS-Co^{II}-sq) / Debye	$\Delta\mu$ / Debye	μ(LS-Co^{III}-cat) / Debye	μ(HS-Co^{II}-sq) / Debye	$\Delta\mu$ / Debye
BuCN	15.92	9.67	-6.25	18.54	11.68	-6.86
DCE	15.52	9.37	-6.15	18.14	11.39	-6.75
DCM	15.41	9.29	-6.12	18.03	11.31	-6.72
Acetone	15.93	9.68	-6.25	18.54	11.69	-6.85

$\Delta\mu$ represents μ(LS-Co^{III}-cat) - μ(HS-Co^{II}-sq)

REFERENCES

1   J. T. Janetzki, F. Z. M. Zahir, R. W. Gable, W. Phonsri, K. S. Murray, L. Goerigk and C. Boskovic, *Inorg. Chem.*, 2021, **60**, 14475–14487.

2   2013.

3   E. Van Lenthe, E. J. Baerends and J. G. Snijders, *J. Chem. Phys.*, 1994, **101**, 9783–9792.

4   M. Douglas and N. M. Kroll, *Ann. Phys.*, 1974, **82**, 89–155.

5   K. Eichkorn, F. Weigend, O. Treutler and R. Ahlrichs, *Theor. Chem. Acc.*, 1997, **97**, 119–124.

6   F. Weigend, M. Häser, H. Patzelt and R. Ahlrichs, *Chem. Phys. Lett.*, 1998, **294**, 143–152.

7   R. Izsák and F. Neese, *J. Chem. Phys.*, 2011, **135**, 144105.

8   H. Nagao, N. Komeda, M. Mukaida, M. Suzuki and K. Tanaka, *Inorg. Chem.*, 1996, **35**, 6809–6815.

9   I. M. Piglosiewicz, R. Beckhaus, G. Wittstock, W. Saak and D. Haase, *Inorg. Chem.*, 2007, **46**, 7610–7620.

10   N. P. Cowieson, D. Aragao, M. Clift, D. J. Ericsson, C. Gee, S. J. Harrop, N. Mudie, S. Panjikar, J. R. Price, A. Riboldi-Tunnicliffe, R. Williamson and T. Caradoc-Davies, *J. Synchrotron Radiat.*, 2015, **22**, 187–190.

11   D. Aragão, J. Aishima, H. Cherukuvada, R. Clarken, M. Clift, N. P. Cowieson, D. J. Ericsson, C. L. Gee, S. Macedo, N. Mudie, S. Panjikar, J. R. Price, A. Riboldi-Tunnicliffe, R. Rostan, R. Williamson and T. T. Caradoc-Davies, *J. Synchrotron Radiat.*, 2018, **25**, 885–891.

12   P. K. Pal, S. Chowdhury, M. G. B. Drew and D. Datta, *New J. Chem.*, 2002, **26**, 367–371.

13   G. M. Sheldrick, .

14   O. V. Dolomanov, L. J. Bourhis, R. J. Gildea, J. A. K. Howard and H. Puschmann, *J. Appl. Cryst.*, 2009, **42**, 339–341.

15   G. M. Sheldrick, *Acta Cryst. A*, 2015, **71**, 3–8.

16   G. M. Sheldrick, *Acta Cryst. C*, 2015, **71**, 3–8.

17   Y. Rechkemmer, J. E. Fischer, R. Marx, M. Dörfel, P. Neugebauer, S. Horvath, M. Gysler, T. Brock-Nannestad, W. Frey, M. F. Reid and J. Van Slageren, *J. Am. Chem. Soc.*, 2015, **137**, 13114–13120.

18   G. A. Bain and J. F. Berry, *J. Chem. Educ.*, 2008, **85**, 532.

19   S. Brahma and R. L. Gardas, *J. Mol. Liq.*, 2018, **256**, 22–28.

20   S. O. Morgan and H. H. Lowry, *J. Phys. Chem.*, 1930, **34**, 2385–2432.

21   M. Chorązewski, E. B. Postnikov, K. Oster and I. Polishuk, *Ind. Eng. Chem. Res.*, 2015, **54**, 9645–9656.

22   C. P. Slichter and H. G. Drickamer, *J. Chem. Phys.*, 1972, **56**, 2142–2160.

23   M. Radoń, *Inorg. Chem.*, 2015, **54**, 5634–5645.

24   G. K. Gransbury, M. E. Boulon, S. Petrie, R. W. Gable, R. J. Mulder, L. Sorace, R. Stranger and C. Boskovic, *Inorg. Chem.*, 2019, **58**, 4230–4243.

25   J. P. Perdew, K. Burke and M. Ernzerhof, *Phys. Rev. Lett.*, 1996, **77**, 3865–3868.

26   A. D. Becke, *Phys. Rev. A*, 1988, **38**, 3098–3100.

27   C. Lee, W. Yang and R. G. Parr, *Phys. Rev. B*, 1988, **37**, 785–789.

28   B. Miehlich, A. Savin, H. Stoll and H. Preuss, *Chem. Phys. Lett.*, 1989, **157**, 200–206.

29   M. Swart, A. R. Groenhof, A. W. Ehlers and K. Lammertsma, *J. Phys. Chem. A*, 2004, **108**, 5479–5483.

30   R. J. Deeth, C. M. Handley and B. J. Houghton, in *Spin-Crossover Materials: Properties and Applications*, ed. M. A. Halcrow, John Wiley & Sons Ltd, 2013, pp. 443–454.

31   C. Adamo and V. Barone, *J. Chem. Phys.*, 1999, **110**, 6158–6170.

32   M. Ernzerhof and G. E. Scuseria, *J. Chem. Phys.*, 1999, **110**, 5029–5036.

33   Y. Zhao and D. G. Truhlar, *Theor. Chem. Acc.*, 2008, **120**, 215–241.

34   T. F. Hughes and R. A. Friesner, *J. Chem. Theory Comput.*, 2011, **7**, 19–32.

35   L. Goerigk, A. Hansen, C. Bauer, S. Ehrlich, A. Najibi and S. Grimme, *Phys. Chem. Chem. Phys.*, 2017, **19**, 32184–32215.

36   L. Goerigk and S. Grimme, *J. Chem. Theory Comput.*, 2010, **6**, 107–126.

37   A. Najibi and L. Goerigk, *J. Chem. Theory Comput.*, 2018, **14**, 5725–5738.

38   D. Sato, Y. Shiota, G. Juhász, K. Yoshizawa, G. Juhász, K. Yoshizawa, G. Juha, K. Yoshizawa, G. Juhász and K. Yoshizawa, *J. Phys. Chem. A*, 2010, **114**, 12928–12935.

39   G. K. Gransbury and C. Boskovic, in *Encyclopedia of Inorganic and Bioinorganic Chemistry*, Wiley, 2021, pp. 1–24.

40   G. K. Gransbury, B. N. Livesay, J. T. Janetzki, M. A. Hay, R. W. Gable, M. P. Shores, A. Starikova and C. Boskovic, *J. Am. Chem. Soc.*, 2020, **142**, 10692–10704.

41   T. T. Patricia, M. V. Sandra, L. Manuela, L. Andrea, F. Paolo, D. Andrea and R. Roberto, *Phys. Chem. Chem. Phys.*, 2012, **14**, 1038–1047.

42   G. E. Douberly, A. M. Ricks, B. W. Ticknor, P. V. R. Schleyer and M. A. Duncan, *J. Am. Chem. Soc.*, 2007, **129**, 13782–13783.

43   K. G. Alley, G. Poneti, P. S. D. Robinson, A. Nafady, B. Moubaraki, J. B. Aitken, S. C. Drew, C. Ritchie, B. F. Abrahams, R. K. Hocking, K. S. Murray, A. M. Bond, H. H. Harris, L. Sorace and C. Boskovic, *J. Am. Chem. Soc.*, 2013, **135**, 8304–8323.

44   A. Dei, A. Feis, G. Poneti and L. Sorace, *Inorg. Chim. Acta*, 2008, **361**, 3842–3846.

45   L. Banci, A. Bencini, C. Benelli, D. Gatteschi and C. Zanchini, in *Structures versus Special Properties*, Springer Berlin Heidelberg, Berlin, Heidelberg, 1982, pp. 37–86.

46   T. Tezgerevska, E. Rousset, R. W. Gable, G. N. L. L. Jameson, E. C. Sañudo, A. Starikova and C. Boskovic, *Dalton Trans.*, 2019, **48**, 11674–11689.

47   A. Beni, A. Dei, S. Laschi, M. Rizzitano and L. Sorace, *Chem. Eur. J.*, 2008, **14**, 1804–1813.

48   C. Benelli, A. Dei, D. Gatteschi and L. Pardi, *Inorg. Chem.*, 1989, **28**, 1476–1480.

49   M. D. Stallings, M. M. Morrison and D. T. Sawyer, *Inorg. Chem.*, 1981, **20**, 2655–2660.

50   D. M. Adams and D. N. Hendrickson, *J. Am. Chem. Soc.*, 1996, **118**, 11515–11528.

51   D. M. Adams, A. Dei, A. L. Rheingold and D. N. Hendrickson, *J. Am. Chem. Soc.*, 1993, **115**, 8221–8229.